CHALMERS
UNIVERSITY OF TECHNOLOGY

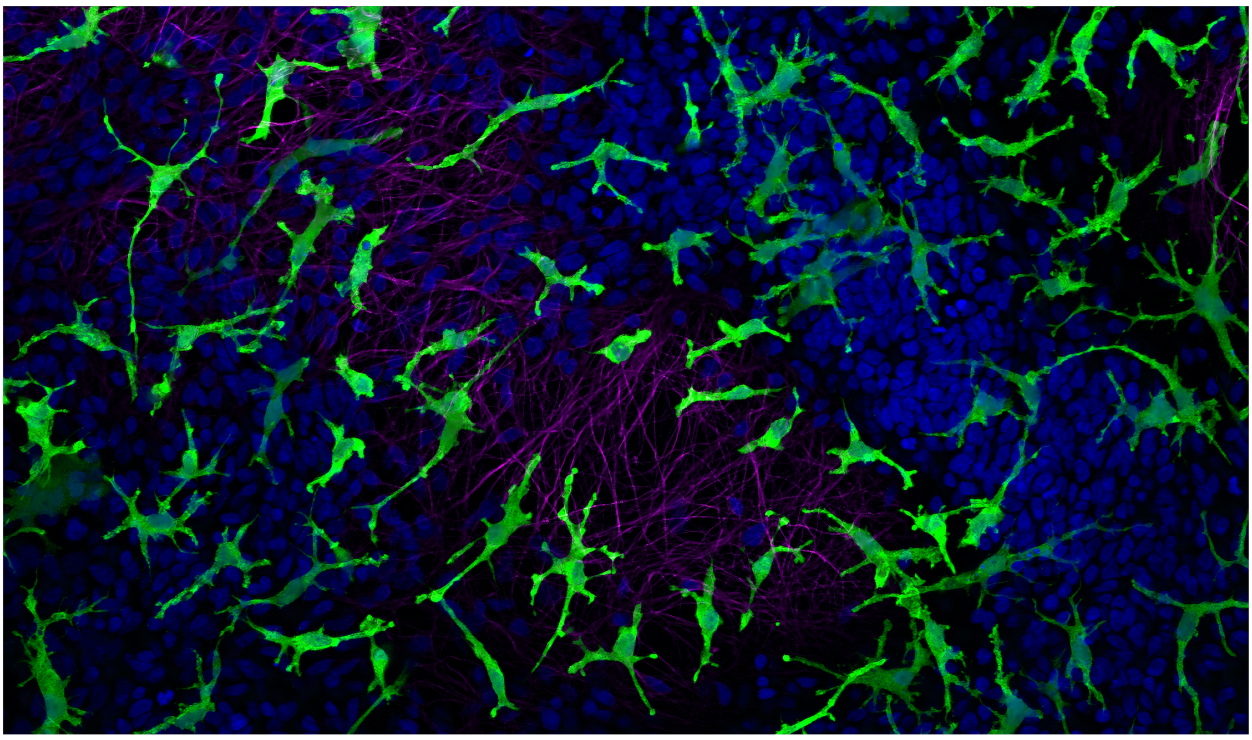

Phenotypic Characterization of a Novel Human Alzheimer's Disease Model to Study Microglia

Characterization of microglial phenotype when cultured in cerebrospinal fluid from Alzheimer's disease patients

Master's thesis in Biotechnology

KAJSA HALLIN & LINNÉA SVÄRD

DEPARTMENT OF LIFE SCIENCE
CHALMERS UNIVERSITY OF TECHNOLOGY
Gothenburg, Sweden 2025
www.chalmers.se

Master's thesis 2025

Phenotypic Characterization of a Novel Human Alzheimer's Disease Model to Study Microglia

Characterization of microglial phenotype when cultured in cerebrospinal fluid from Alzheimer's disease patients

KAJSA HALLIN & LINNÉA SVÄRD

CHALMERS
UNIVERSITY OF TECHNOLOGY

Department of Life Science
Division of Chemical Biology
Research group of Stefanie Fruhwürth
Chalmers University of Technology
Gothenburg, Sweden 2025

Phenotypic Characterization of a Novel Human Alzheimer's Disease Model to Study Microglia
Characterization of microglial phenotype when cultured in cere- brospinal fluid from Alzheimer's disease patients
KAJSA HALLIN & LINNÉA SVÄRD

Supervisor: Christina Heiss, Sahlgrenska Academy
Examiner: Pernilla Wittung Stafshede, Department of Life Science

Master's Thesis 2025
Department of Life Science
Division of Chemical Biology
Chalmers University of Technology
SE-412 96 Gothenburg
Telephone +46 31 772 1000

Cover: A coculture containing microglial cells and cortical neurons cultured in non-AD cere-brospinal fluid for 24 hours.

Phenotypic Characterization of a Novel Human Alzheimer's Disease Model to Study Microglia
Characterization of microglial phenotype when cultured in cerebrospinal fluid from Alzheimer's disease patients
KAJSA HALLIN & LINNÉA SVÄRD
Department of Life Science
Chalmers University of Technology

Abstract

Alzheimer's disease (AD) is the most prevalent form of dementia and accounts for approximately 60-70% of all dementia cases [1]. The pathological hallmarks of AD include the accumulation of amyloid-β plaques and tau tangles [1]. In addition to these hallmark features, neuroinflammation plays a crucial role in the progression of the disease [2]. Microglial cells, the brain's resident immune cells, are key players in neuroinflammatory processes [2]. In response to external and internal stimuli, they transform into different states, each characterized by distinct phenotypic changes [2]. Given their central role in mediating neuroinflammation and their sensitivity to disease-related biomarkers, it is expected that AD significantly influences the microglial phenotype.

In this study, we developed and evaluated a novel human cell model to investigate changes in microglial phagocytic activity, gene expression, and morphology when cultured in cerebrospinal fluid (CSF) derived from AD patients. Human-induced pluripotent stem cell-derived microglia and cortical neurons were seeded into monocultures and cocultures, followed by incubation in CSF from AD and non-AD (CTRL) patients. The cell model was then analyzed using various functional assays, qPCR, and a morphology analysis pipeline for ImageJ and RStudio.

The results showed that CSF exposure had no adverse effects on microglial viability or proliferation, supporting the model's robustness. While qPCR and phagocytosis assays indicated increased activation in AD-CSF-treated microglia compared to CTRL-CSF, no morphological differences were observed between these groups. Instead, pronounced differences in morphology were detected between the CSF-treated and coculture media (CoM) treated conditions, highlighting the influence of CSF-derived substances on microglial morphology. These results demonstrate that the cell model can be used to study microglial phenotypic changes when cultured in AD-CSF and CTRL-CSF. However, additional analyses are needed to detect morphological differences between microglia exposed to AD- and CTRL-CSF.

Acknowledgements

We would like to express our gratitude and appreciation to our supervisor, Christina Heiss, for her guidance, support, and encouragement throughout the development of this thesis. Her expertise and feedback greatly enhanced the quality of this work. Special thanks also go out to the entire research group at Sahlgrenska for sharing their knowledge and assistance with protocols, support, and guidance during the experiments.

We also wish to thank our examiner, Pernilla Wittung Stafshede, for her constructive input and inspiring discussions.

We gratefully acknowledge the support provided by Chalmers University of Technology and the Department of Life Sciences.

Finally, we would like to thank our families and friends for their patience, encouragement, and continuous support throughout this journey.

Kajsa Hallin & Linnéa Svärd, Gothenburg, June 2025

List of acronymes

Aβ	Amyloid-beta
ACTB	Actine beta
AD	Alzheimer's disease
APOE	Apolipoprotein E
APP	Amyloid precursor protein
C1QA	Complement C1q A Chain
CD68	Cluster of Differentiation 68
CNS	Central nervous system
CoM	Coculture media
CTRL	Human control CSF (non AD-CSF)
CSF	Cerebrospinal fluid
DAM	Disease-associated microglia
DAPI	4′,6-diamidino-2-phenylindole
DMEM	Dulbecco's Modified Eagle Medium
EB	Embryonic body
EBM	Embryonic body media
EDTA	Ethylenediaminetetraacetic acid
hiPSC	Human induced pluripotent stem cell
Iba1	Ionized calcium-binding adaptor molecule 1
Ki67	Kiel 67
LDH	Lactate dehydrogenase
M1	pro-inflammatory state
M2	anti-inflammatory state
MAPT	Microtubule-Associated Protein Tau
MiM	Microglial maintenance media
mPTP	Mitochondrial permeability transition pore
mTesR+	Maintenance Trophoblast stem cell Renewal +
NDD	Neurodegenerative disease
NIM	Neural induction media
NMM	Neural maintenance media
NPC	Neural progenitor cell
NULISA	Nucleic acid-Linked Immuno-Sandwich Assay
PBS	Phosphate-Buffered Saline
PLO	Poly-L-Ornithine
PMP	Primitive macrophage precursor
PNS	Peripheral nervous system
ROS	Reactive oxygen species
TNF	Tumor necrosis factor
TMEM119	Transmembrane protein 119
TUJ1	Neuron-specific class III beta-tubulin
QQ	Quantile-Quantile

Contents

1 Background

Neurodegenerative diseases (NDDs) are disorders that affect neurons in both the central nervous system (CNS) and the peripheral nervous system (PNS), leading to their gradual degeneration and loss of function [3]. As neurons are highly specialized cells that do not easily regenerate, their breakdown disrupts essential communication pathways in the nervous system, resulting in memory loss and impaired sensory and motor function [3].

One of the key hallmarks of NDDs is protein aggregation [3]. Proteins play a fundamental role in maintaining the physiological function of cells, and their function depends on their structural state [4]. Proteins can exist in different conformations and sizes, and under pathological conditions, they may adopt abnormal solid states that affect their function [4]. In NDDs, amyloid proteins are commonly involved [5]. These are aggregated protein species characterized by a distinctive β-sheet-rich fibrillar structure [6]. Although the precise mechanisms underlying disease progression remain unclear, growing evidence suggests that toxicity arises, either directly or indirectly, from the formation of these amyloid aggregates [5].

Amyloid formation is influenced by several factors, including the thermodynamic stability of different protein states, the energy barriers between these states, the total protein concentration, and cellular processes such as protein synthesis, degradation, chaperone activity, post-translational modifications, and chemical transformations [4]. The specific type of amyloid aggregates formed depends on the particular NDD [3]. In Alzheimer's disease (AD), the most prominent aggregates are amyloid-β plaques (Aβ plaques) and tau tangles, which are described in more detail below.

1.1 Alzheimer's disease

AD is a neurodegenerative disorder and the most common form of dementia, accounting for approximately 60–70% of all dementia cases [1]. While memory loss is a hallmark symptom, individuals with AD also commonly experience impairments in other cognitive domains, such as difficulties finding words, trouble interpreting visual information, and reduced reasoning and judgment abilities [7]. As mentioned in section 1, NDDs lead to the gradual degradation of neurons and ultimately cell death. However, in AD, synaptic dysfunction can be seen even before noticeable neuronal loss occurs [3].

1.1.1 Synaptic dysfunction and neural cell death

Several mechanisms contribute to synaptic dysfunction and eventually cell death in AD, including excitotoxicity, energy depletion, and lysosomal dysfunction [3]. Excitotoxicity happens when neurons become overactive and absorb excessive amounts of calcium. This calcium overload damages the mitochondria, causing the opening of the mitochondrial permeability transition pore (mPTP), which then activates different types of enzymes. These enzymes can trigger either apoptosis or necrosis. Energy depletion occurs when neurons are deprived of oxygen and glucose, leading to a rapid reduction in adenosine triphosphate (ATP) production. As a result, the plasma membrane loses its ability to maintain the ion balance, which causes excessive release of glutamate, a neurotransmitter that becomes toxic at high levels [3]. Lysosomal damage leads to the rupture of lysosomes, releasing different types of enzymes into the cell. These enzymes degrade essential cellular components and contribute to the accumulation of toxic protein aggregates, including Aβ plaques and tau tangles [3].

Mitochondrial damage can lead to an accumulation of reactive oxygen species (ROS), as impaired cells are less capable of managing and neutralizing ROS compared to healthy ones [8]. Excessive ROS levels can damage DNA, lipids, and proteins, making neurons more vulnerable to further injury. This oxidative stress also contributes to the misfolding and aggregation of Aβ plaques and tau tangles [8]. In addition, metal ion imbalance in the brain has also been linked to increased ROS production. Metals such as iron, zinc, copper, and manganese play essential roles in growth, metabolism, and brain development [9]. However, when the concentrations of these elements become dysregulated, they can promote protein misfolding and aggregation, trigger oxidative stress, and contribute to neuroinflammation and neuronal loss [9].

1.1.2 Amyloid-βnd tau tangles

As previously mentioned, AD is characterized by the accumulation of Aβ plaques and abnormal tau tangles [1]. Aβ plaques are a result of an imbalance between the production and clearance of Aβ peptides [10]. The amyloid precursor protein (APP) is a membrane-bound glycoprotein involved in several biological processes, including neural development and signaling [11]. There are two different processing pathways of APP called amyloidogenic processing and non-amyloidogenic processing [12]. In the amyloidogenic pathway, APP is cleaved by β-secretase and γ-secretase to produce Aβ monomers [12]. The aggregation of Aβ in the brain promotes the formation of amyloid plaques, a hallmark of AD. In contrast, the non-amyloidogenic pathway involves cleavage by α- and γ-secretase, which does not generate Aβ [12]. When the amyloidogenic pathway is active and Aβ monomer concentrations become too high, these monomers begin to aggregate into Aβ oligomers, which can further assemble into fibrils and eventually form insoluble Aβ plaques (see image *A* in Figure 1) [10]. Among these different forms of Aβ, Aβ oligomers are thought to have the strongest toxicity to neurons [1]. The cleavage of APP produces several different isoforms of Aβ, including Aβ38, Aβ40, and Aβ42. Among these, Aβ42 has the highest tendency to aggregate, and it is the predominant isoform found in Aβ plaques [13].

Furthermore, tau tangles are formed by the aggregation of the tau protein, and their formation is accelerated by the accumulation of Aβ fibrils [14]. Under normal physiological conditions, tau stabilizes microtubules and helps to maintain DNA structure. However, in AD, tau undergoes hyperphosphorylation, which decreases its affinity for microtubules and causes it to detach (see image *B* in Figure 1) [1]. The tau protein is encoded by the Microtubule-Associated Protein Tau (*MAPT*) gene and exists in different types of isoforms. However, when the tau protein becomes hyperphosphorylated, it forms phosphorylated variants such as phosphorylated at threonine 181 (pTau181), phosphorylated at threonine 217 (pTau217), and phosphorylated at threonine 231 (pTau231). These forms are strongly associated with AD and can be detected in the blood and cerebrospinal fluid (CSF) of individuals with AD [15]. The accumulation of these proteins can lead to synaptic dysfunction, loss of neuronal function, and the aggregation of tau into tangles [1].

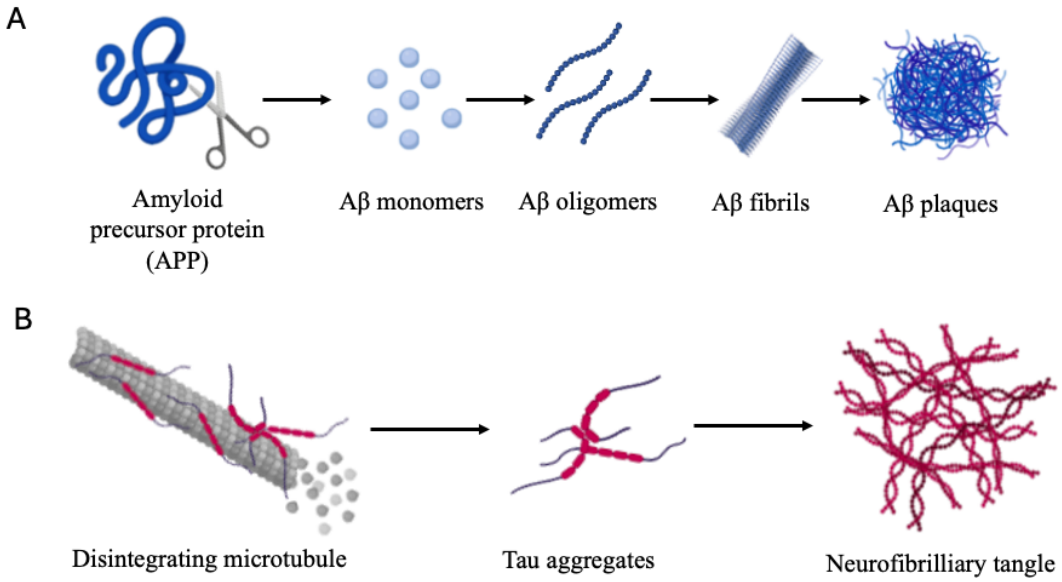

Figure 1: ***A)*** Aβ plaque formation steps. APP is cleaved to produce Aβ monomers. When the concentration of these monomers becomes too high, they begin to aggregate into Aβ oligomers, which can further form fibrils and eventually insoluble Aβ plaques (Illustration created using Biorender). ***B)*** Tau tangle formation steps. Tau undergoes hyperphosphorylation which decreases its affinity for microtubules and causes it to detach (Illustration created using BioRender).

1.2 Microglial cells

Although Aβ plaques and tau tangles are two pathological hallmarks of AD, these alone cannot explain the disease's pathogenesis [1]. Elevated levels of inflammatory markers in AD patients suggest that neuroinflammation plays a significant role in AD pathogenesis [1]. Microglial cells, the primary immune cells of the brain, play a central role in mediating this neuroinflammatory response [16]. Functionally similar to macrophages, microglia eliminate harmful substances and contribute to the maintenance of brain homeostasis [16]. They support neuronal survival and differentiation through selective remodeling, a process by which they engulf damaged or unnecessary synapses, myelin, and extracellular matrix components. [16]. When microglial function is disrupted or chronically activated, this delicate balance may be disturbed, leading to damage to the CNS [17].

Microglial cells have a complex series of surface receptors that allow them to adopt different types of states in response to various internal or external stimuli [2]. They have long been categorized into two opposing phenotypic states: classical pro-inflammatory state (M1) and alternative anti-inflammatory state (M2) [2]. However, recent studies have demonstrated that microglial cells do not strictly polarize into either the M1 or M2 phenotype but instead often co-express markers of both states simultaneously [2]. Furthermore, in reality, microglial cells can exhibit various intermediate states between these two phenotypes [18]. Depending on specific signals or challenges in the CNS, the microglial cells will change their signature through the stages of life, from development to aging [2].

The homeostatic state refers to a non-active or a surveillant microglia state. However, even in the homeostatic state, the microglial cells display diverse morphological and functional states depending on signals from the CNS environment [2]. Recent scientific advances have identified a novel subpopulation of microglia linked to neurodegenerative diseases, known as disease-associated microglia (DAM) [18]. During the progression of AD, the homeostatic microglial signature is down-regulated, causing microglial cells to transition to the DAM state [18]. Studies have shown that only a subset of microglial cells transition into this state, and this transition is correlated with the amount of Aβ plaques present [16]. The DAM state is observed only in microglial cells located near Aβ plaques, suggesting that the microenvironment surrounding the plaques plays a key role in driving this phenotypic shift [16]. Some of the features of the DAM state are microglia involvement in cytokine and chemokine production, activation of phagocytosis, and generation of ROS [3]. In response to danger signals, microglia secrete ROS, which contributes to oxidative damage and disrupts homeostasis in the brain [3]. Additionally, microglia secrete both pro-inflammatory and anti-inflammatory cytokines, which either promote or suppress inflammation [16]. Under normal conditions, the inflammatory response of microglial cells is typically resolved after they have carried out their function [3]. However, if the inflammatory response persists, it can lead to chronic inflammation, which may, in turn, contribute to the progression of AD [3].

During the transition from a homeostatic to a reactive state, microglial proliferation increases [19]. Under normal physiological conditions, microglia divide at a relatively slow rate, with a median turnover of approximately 28 % per year, and some cells have been shown to persist for over two decades [20]. However, during disease progression, microglial cells become activated and start to proliferate more rapidly, producing daughter cells in response to pathological stimuli [19].

During disease progression, Transmembrane protein 119 (*Tmem119*), a microglia-specific gene often associated with AD in humans, is upregulated in activated microglia during AD [21]. Additionally, inflammatory genes such as Apolipoprotein E (*APOE*) and Complement C1q A Chain (*C1QA*) are upregulated during microglial activation [16]. Both genes are strongly associated with neuroinflammation and have been linked to a variety of neurodegenerative diseases [22, 23]. Lastly, Cluster of Differentiation 68 (*CD68*), a marker of macrophages and phagocytic activity, is also upregulated in activated microglia and serves as an indicator of their increased ability to engulf debris and pathological proteins [24].

1.2.1 Microglial morphologies

The function of various microglial states and their impact on AD are still unclear [24]. However, scientific advancements have demonstrated that differences in morphology, gene expression, and metabolic activity can distinguish these states [24]. Based on the compactness or branching of their morphology, microglial cells can be associated with different functional states [25]. For this study, the four morphologies described below are the primary focus. However, in reality, a range of intermediate microglial morphologies exists [24].

In the homeostatic state, microglia typically exhibit a branched and complex morphology, commonly referred to as the ramified form (see Figure 2) [24]. During the progression of AD, the microglial cells become swollen, with larger cell bodies and fewer branches [25]. This results in an ameboid morphology frequently associated with increased phagocytic activity. Ameboid microglia are commonly observed in conditions of severe or chronic inflammation, where retraction of branches enhances both their phagocytic capacity and motility toward sites of damage [24].

In addition to these forms, other morphologies are also linked to reactive microglial states. The hypertrophic morphology, which is considered intermediate between ramified and ameboid forms, is characterized by a large cell body and short, thick branches (see Figure 2) [24]. Another form, rodlike microglia, has not yet been associated with a specific function [24]. However, an increase of rodlike microglia in the brain has been observed with aging [2]

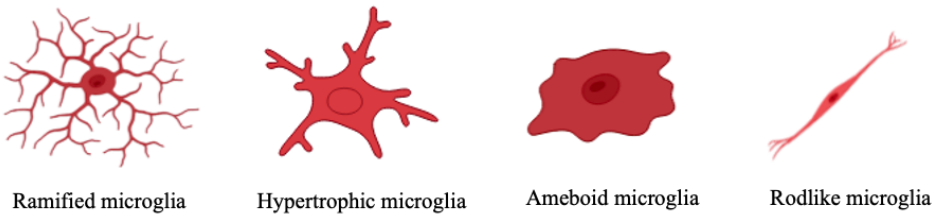

Figure 2: Micoglia morphologies associated with microglia states (Illustration created using BioRender).

1.3 Cortical neurons

The brain's structure, known as the neocortex, is believed to be the reason behind our unique cognitive abilities [26]. It contains various classes of cortical neurons, categorized depending on criteria like morphology, gene expression profile, long-range connectivity, and developmental history [26]. These neurons fall into two major groups: pyramidal neurons, which are highly polarized and responsible for long-range cortical communication; and interneurons, which are typically multipolar, inhibitory, and play key roles in regulating local circuit activity [27, 28]. Interneurons exist to carry sensory information as well as regulate motor activity [27, 28]. Pyramidal neurons can be further divided into subtypes depending on morphology and laminar connectivity [27]. Regardless of their subcategory, all pyramidal neurons share two main functions: transmitting excitatory signals and intracortical communication through their branches [27].

In AD, changes in the neocortex have been observed, like altered neuronal complexity and synaptic loss [29]. It has been shown that patients with AD have an increased complexity in the frontal and temporal cortex, while the complexity is decreased in the insula cortex [29]. These structural alterations may be linked to chronic neuroinflammation, which arises from prolonged activation of the brain's immune response [30].

1.4 Cerebrospinal fluid

CSF is a clear fluid that circulates within the brain and spinal cord, where it serves as both a protective cushion and a medium for clearing metabolic waste from the CNS [31]. During the progression of NDDs, the composition of substances in the CSF changes, reflecting underlying pathological processes in the brain [32]. In AD, two core biomarkers are commonly assessed in CSF, $A\beta 42$ and tau tangles. Several diagnostic methods exist to detect AD, including direct sampling of CSF using a spinal tap to measure these biomarkers [33]. In both clinical diagnostics and translational research, CSF biomarkers such as $A\beta 42$ and tau tangles have become important for identifying and characterizing AD pathology [34].

2 Aim and objectives

The project aims to identify AD-specific microglial phenotypes by analyzing their altered gene expression, phagocytic activity, and morphology. The following objectives will help to achieve this aim.

1. Set up monocultures of microglia and culture them in patient-derived CSF, and validate the cell cultures using a cell viability assay, cytotoxicity assay, and Kiel 67 (Ki67) staining.

2. Analyze the differences in protein abundance in patient-derived AD- and CTRL-CSF using NUcleic acid-Linked Immuno-Sandwich Assay (NULISA).

3. Determine the gene expression for *APOE*, *C1QA*, *TMEM119* and *CD68* in microglia cultured in patient-derived AD- and CTRL-CSF.

4. Determine the difference in phagocytic ability of microglial cells cultured in patient-derived AD- and CTRL-CSF.

5. Determine the morphology of microglial cells cultured together with cortical neurons in patient-derived AD- and CTRL-CSF using the image analysis tool ImageJ and analyze the obtained data with RStudio.

3 Methods

This analysis is performed on microglial cells derived from human induced pluripotent stem cells (hiPSCs) cultured in CSF from AD patients and non-AD (CTRL) patients. Below, the seeding and preparation of cell cultures are described as well as the methods for analyzing the resulting changes in phenotype.

3.1 Seeding and preparation of cell cultures

In this study, both monocultures of microglial cells and cocultures of microglial cells and cortical neurons were used. Cocultures were employed exclusively for the morphology analysis, as the presence of cortical neurons helps to spatially separate the microglial cells, making it easier to study their morphology. For all the other experiments, including functional assays and qPCR, monocultures of microglial cells were used. The microglial cells and cortical neurons used throughout the study were derived from the hiPSC lines WTSLi015-A (obtained from EBiSC through Sigma-Aldrich) and CTRL1 (obtained from the Selina Wray lab). The WTSLi015A hiPSCs were used for the experiments unless stated otherwise. Both hiPSCs have received ethical approval before use by the companies. The procedures for cell differentiation and culture preparation are described in the following sections.

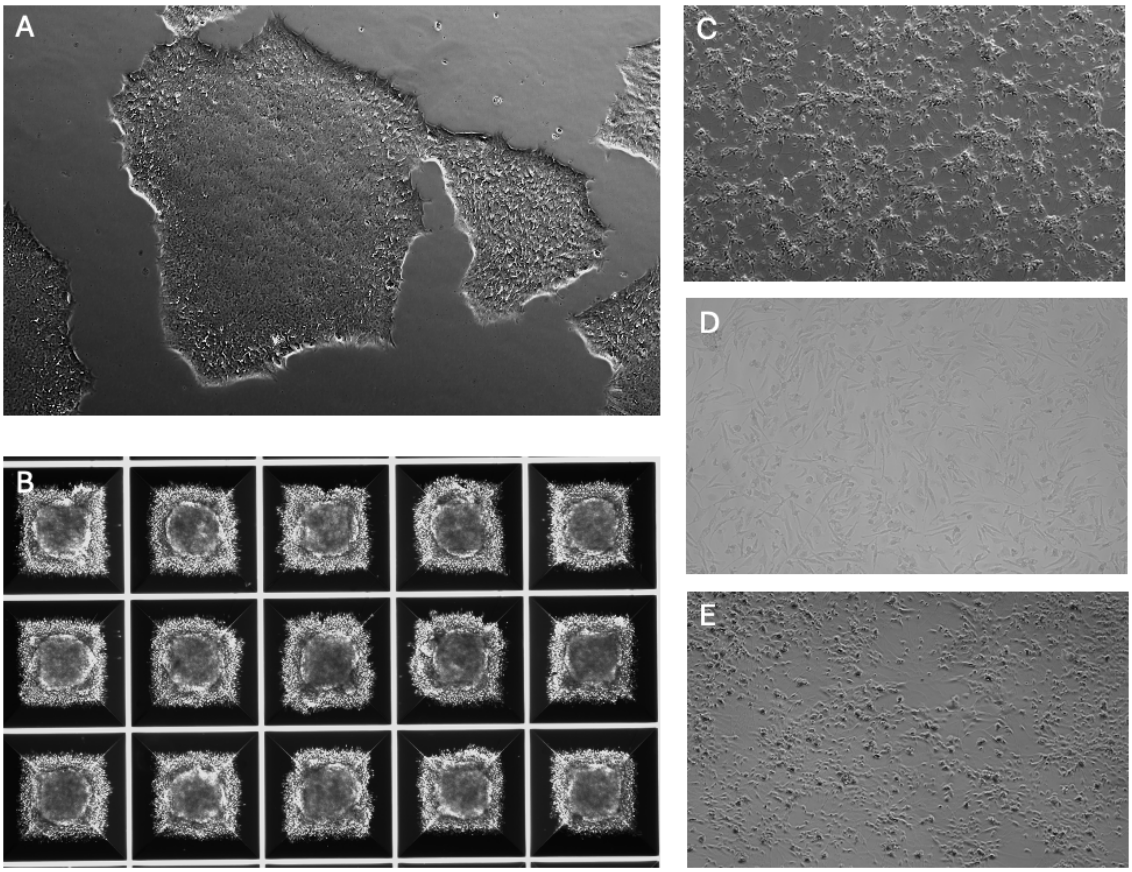

Figure 3: ***A)*** hiPSCs cultures in mTesR+ (passage number 45). ***B)*** EB formation in AggreWells cultured in embryoid body medium (EBM). ***C)*** Differentiated cortical neurons on day 46, cultured in neural maintenance media (NMM). ***D)*** Differentiated microglial cells cultured in microglia media (MiM). ***E)*** Coculture containing differentiated cortical neurons (day 52) and microglial cells cultured in coculture media (CoM).

3.1.1 Microglial cell differentiation

First, the hiPSCs were thawed and cultured in mTeSR1 according to an established protocol by Shi et al. [35]. During the initial phase of differentiation, the cell media was changed daily and the cells were passaged upon reaching 80% confluency (see plot *A* in Figure 3). After about two weeks in culture, the hiPSCs were detached from the wells using TrypLE Express, and the single cells were then seeded into AggreWells to form embryonic bodies (EBs) (see Figure 3). The formation process took five days, during which embryroid body media (EBM) was added to the culture to promote the development of EBs. The EBs were then harvested and transferred to well plates to develop primitive macrophage precursors (PMPs) (see Figure 4). In this step, hematopoietic media (HM) was added to the culture. After about four weeks, the PMPs were ready to be harvested to produce microglia cells. Firstly, the PMPs were collected and counted from two wells. For the described experiments, 50,000 microglial cells/cm^2 were seeded into each well. The cells were then incubated for at least 45 minutes before the culture media was replaced with fresh microglia media (MiM) (see Figure 3). The culture media was then changed every other day.

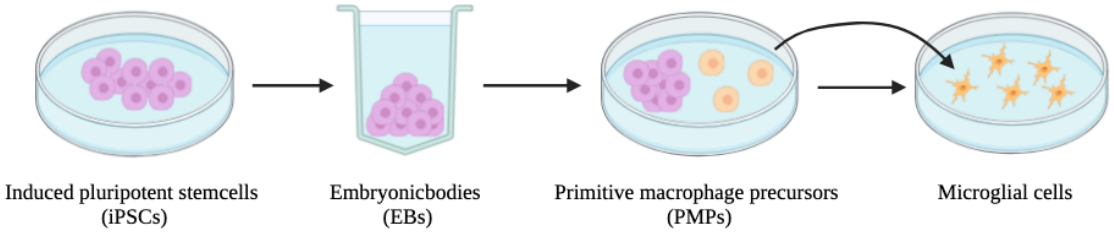

Figure 4: The differentiation of microglial cells involves several key steps. First, hiPSCs are cultured and then transferred to AggreWell plates to form EBs. These EBs are subsequently transferred to standard culture plates, where they give rise to PMPs. Finally, the PMPs are transferred to new plates to differentiate into mature microglial cells (Illustration created using BioRender).

3.1.2 Cortical neuron differentiation

The differentiation from hiPSCs to neural progenitor cells (NPCs) was performed using a protocol established by Shi et al [35]. First, the hiPSCs were thawed and cultured in mTeSR1. Cells from two wells, each at 70–80 % confluency, were collected using EDTA and then transferred to a Matrigel-coated 6-well plate in mTeSR medium supplemented with ROCK inhibitor. On day 0, neural induction media (NIM) supplemented with Dorsomorphin and SB431542 was added to initiate differentiation. The cells were then cultured and passaged according to the established protocol. After approximately 7 days, the medium was switched to neural maintenance media (NMM) supplemented with FGF2. Around day 13, neural rosettes began to form (see Figure 5). Between days 20 and 30, these neural rosettes started producing NPCs, which were then frozen for future use.

The steps described above were performed by other researchers in our group. Our contribution began with thawing the NPCs between days 28 and 32. The cells were then cultured for an additional 2–3 weeks to generate cortical neurons, with the culture medium being changed every other day, and passages being done when cells reached confluency (see Figure 3).

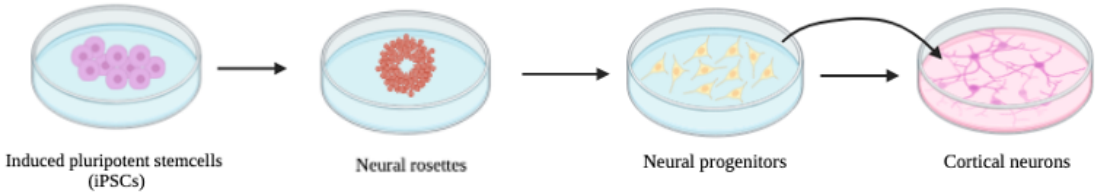

Figure 5: The differentiation of cortical neurons from hiPSCs involves several stages. Initially, hiPSCs form neural rosettes, which subsequently give rise to neural progenitor cells. These progenitors then produce cortical neurons (Illustration created using BioRender).

3.1.3 Cell culturing

To coat the wells before adding passaged cortical neurons, 1 mL of sterile Phosphate-Buffered Saline (PBS) (+/+) was mixed with 50 μL of Biolamina and added to a 6-well plate. The plate was then incubated at 37°C for two hours or stored in the fridge overnight. For seeding cortical neurons, a glass coverslip was first put into each well, followed by adding the coating consisting of 500 μL of PBS (+/+) and 5 μL of Poly-L-Ornithine (PLO). This was followed by overnight incubation in the fridge. The following day, the plate was coated once more with 1 mL of PBS (+/+) and 50 μL of Biolamina followed by incubation at 37°C for two hours. When coating the wells before adding passaged hiPSCs, 15 μL of Matrigel was mixed with 1 mL of Dulbecco's Modified Eagle Medium (DMEM). The plate was then incubated at room temperature for at least one hour.

For passaging of the hiPSCs, a protocol from the European Bank for hiPSCs was used [35]. Firstly, the media was removed from the wells containing hiPSCs and washed once with 2 ml PBS (-/-). 1 ml of 0.5 mM EDTA was added and the plate was incubated for 3-5 minutes at 37°C. When the cells started to detach from the bottom of the wells, the EDTA was carefully removed, and 1 ml of room-tempered mTeSR+ media was added. The cells were then collected and gathered into a tube. The Matrigel was removed from the coated plate, and the appropriate amount of media was added to ensure a final volume of 2 ml per well after cell addition. The cells were then added to the wells.

For passage of cortical neurons, the following method was used. Initially, the cells were washed with 1 mL of PBS (+/+) before adding 500 μL of Accutase. The plate was then incubated at 37°C for five minutes. After incubation, the cells were transferred to a tube containing 10 mL of working solution (5 mL DMEM and 5 mL Neurobasal). The tube was then centrifuged at 400xg for 5 minutes, and the supernatant was discarded. The cell pellet was resuspended in 10 mL of working solution and centrifuged again at 400xg for 5 minutes. After the second centrifugation, the supernatant was removed, and either 2 mL or 4 mL of NMM was added to the cell pellet, depending on whether a 1:1 or 1:2 passage was performed. The cells were then transferred to a coated 6-well plate (see coating protocol above) and placed in the incubator. The NMM was changed the day after passaging and subsequently every other day.

To fixate the cells, they were washed for one minute with phosphate-buffered saline (PBS). Histofix was then added to each well, followed by incubation at room temperature for ten minutes. The histofix was removed, and PBS was then added to the wells. The fixed cells were then stored in the fridge until further use.

3.1.4 Cocultures

The cortical neurons were differentiated as described in section 3.1.2. NPCs were seeded into 24-well plates using NMM as the culture medium. Once the cortical neurons covered approximately 70 % of the well surface, PMPs were added to the cultures. This was done by collecting PMPs from two separate wells in the PMP plate. The collected PMPs were centrifuged at 400xg for three minutes, after which the supernatant was discarded and the cell pellet was resuspended in coculture media (CoM). The PMPs were then added to the wells containing cortical neurons. The CoM was changed the following day and subsequently every other day. After approximately 5–7 days in culture, the cocultures were ready for use in experiments (see Figure 3). When adding CSF to the cocultures, approximately 200 μL was added to the 48-well plates and 300 μL to the 24-well plates.

3.2 CSF pools

The CSF used in this study was collected from a patient cohort at Mölndal Hospital, with appropriate ethical approval. The samples were obtained from a previously conducted collection, and we were provided with leftover CSF that was not intended for any other use. From an ethical standpoint, this means that we utilized material that would otherwise have been discarded. The cohort included both CSF from patients diagnosed with AD and non-AD patients (CTRL). Before our thesis work began, five pools for each group were prepared (AD and CTRL), with each pool containing equal volumes of CSF from five different individuals. The grouping of samples into the AD and CTRL-pools was based on tau concentration, where CSF with similar tau concentrations was grouped together. All CSF samples were stored at –80°C before use in experiments. In all experiments where CSF was used, it was supplemented with 1 μL/mL of the factors IL-34 and GM-CSF. To validate the grouping and confirm differences in protein abundance between the AD and CTRL-group, the pooled CSF was analyzed using NULISA. The details of this procedure are described below.

3.2.1 NUcleic acid Linked Immuno-Sandwich Assay

NULISA is a technique that offers a multiplexed quantification of both low- and high-abundance proteins in a solution by reducing the signals from abundant targets with unconjugated antibodies and with next-generation sequencing [36]. In this study, the ten CSF-pools (five CTRL-pools and five AD-pools) were sent to the hospital in Mölndal for NULISA analysis. The resulting protein expression data were returned and further analyzed using RStudio [37]. To assess the distribution of each protein, Quantile-Quantile (QQ) plots were generated to evaluate normality. The difference in abundance of different proteins in the AD- and CTRL-pools was assessed using a volcano plot based on p-values. The proteins identified as significant were further corrected for multiple comparisons using false discovery rate (FDR) adjustment. Furthermore, a heatmap was generated to visualize the top 20 proteins with the highest difference in abundance between the AD and CTRL-pools. Additionally, a principal component analysis (PCA) plot was generated to illustrate the differences between the CTRL- and AD-pools based on overall protein expression profiles.

3.3 Experimental validation of the cell model

To evaluate the cell model, a series of functional assays and a Ki67 staining were performed. These experiments evaluated cell viability, cytotoxicity, and proliferation within the model. The methods are described below.

3.3.1 Cell viability assay

First, a cell viability assay was conducted on the microglial cells to assess how being cultured in CSF affected their viability. The cells were added to a 96-well plate, and after four days in culture, the experiment began. Two tubes were prepared, one containing CTRL-CSF and one containing AD-CSF. Later, 70 μL of MiM or CSF were added to each well (see plate layout in Figure A1 in the appendix). The cells were then incubated at 37°C for 24 hours. For the assay, a CyQUANT™ XTT Cell Viability Assay kit from ThermoFisher SCIENTIFIC was used [38]. In the assay, metabolic activity was assessed by measuring the conversion of a chemical into a colored compound. Higher absorbance (more intense color) indicated more actively respiring cells and therefore higher viability. Firstly, the XTT reagent was thawed in a 37°C water bath, and the electron coupling reagent was thawed at room temperature. Both reagents were then mixed in a vortex until fully homogeneous. The XTT reagent and the electron coupling reagent were then added to a tube in a ratio of 6:1. The solution was then mixed and added to the plate with microglial cells (70 μL/well). The plates were then incubated in an incubator (37°C) for 1 hour and 45 minutes, after which the absorbance was read in a plate reader at wavelengths 450 nm and 660 nm. The experiment was conducted having five replicates for each group (MiM, CTRL-CSF, and AD-CSF).

3.3.2 Cytotoxicity assay

Complementary to the cell viability assay, a cytotoxicity assay was conducted to evaluate the quality of the cell model. For this analysis, a CyQUANT™ LDH Cytotoxicity Assay kit from ThermoFisher SCIENTIFIC was used [39]. Cell death was assessed by measuring the concentration of lactate dehydrogenase (LDH), an enzyme that leaks out of dying or damaged cells, where a high absorbance indicated a greater number of dead or damaged cells. Microglial cells were seeded out in a 96-well plate, and after four days in culture, the experiment began. Two tubes were prepared, one containing CTRL-CSF and one containing AD-CSF. Additionally, a tube containing phenolred-free MiM was prepared by mixing 5 mL phenolred-free DMEM, 10 μL sodium pyruvate, 10 μL PEST, 1.1 μL mercaptoethanol, 1 μL IL34, and 1 μL GM-CSF.

Later, 70 μL of MiM (phenol red-free) and the two tubes with CSF were added to the wells according to Figure A2. The plate was then incubated for 24 hours. On the day of the experiment, 10 μL of sterile, ultrapure water was added to the spontaneous LDH activity wells (see Figure A2, and 10 μL of 10X Lysis Buffer was added to the maximum LDH activity wells. The plate was then incubated for 45 minutes at 37°C. 50 μL of each sample medium was then transferred to a new black 96-well flat-bottom plate. 50 μL of 1X LDH Positive Control was added into three wells in the new plate (wells containing no cells). 50 μL of Reaction Mixture was added to each sample well and mixed well. The plate was then incubated at room temperature for 30 minutes in the dark. 50 μL of Stop solution was then added to all wells, and the absorbance was measured at 490 nm and 680 nm. The cytotoxicity was then calculated using Equation 1. The experiment was conducted having five replicates for each group (MiM, CTRL-CSF, and AD-CSF).

$$\text{Cytotoxicity } (\%) = \frac{LDH_{\text{experimental}} - LDH_{\text{spontaneous}}}{LDH_{\text{maximum}} - LDH_{\text{spontaneous}}} \cdot 100 \tag{1}$$

3.3.3 Cell division analysis

Another way to evaluate the quality of the cell model was to measure cell division in the microglial cell cultures. This was done using the primary antibody Ki67. Microglial cells were seeded in six wells in a 48-well plate. Four days after seeding, two tubes were prepared, one containing CTRL-CSF and one containing AD-CSF. MiM, CTRL-CSF, and AD-CSF were then added to the wells (duplicates for each group). After 24 hours, the cells were fixed and stained using Ki-67 as the primary antibody (diluted 1:400 in TBS) for the staining of dividing cells and Iba-1 (diluted 1:500 in TBS) for the staining of microglial cells. Anti-mouse was used as the secondary antibody and 4',6-diamidino-2-phenylindole (DAPI) for cell nuclei staining (see section 3.1.3 for further description). Pictures were then taken of the microglial cells using a confocal microscope. The percentage of nuclei divisions per well could then be calculated using a pipeline in ImageJ [37].

3.4 qPCR

After analyzing the cell model and the CSF, the experiments on the cell model were initiated. First, a qPCR was performed to measure the gene expression of *TMEM119*, *APOE*, *C1QA*, and *CD68*. Below is a description of a qPCR procedure on cDNA samples from microglia cultured in CSF for 24 hours.

After the 24-hour incubation, the cells were lysed and RNA was extracted using the RNeasy Mini Kit following the manufacturer's instruction. These steps had been done by our supervisor beforehand and will therefore not be described in further detail here. The extracted RNA was then converted into cDNA. First, the RNA samples were diluted with RNase-free water to a total volume of 9 μL. Then, 1 μL of enzyme and 10 μL of Mix from a High-Capacity RNA-to-cDNA Kit from Thermo Fisher Scientific were added to each tube, resulting in a final volume of 20 μL. Lastly, the samples were put in a thermal cycler for 1 hour and 20 minutes.

After converting the RNA to cDNA, the qPCR could begin. First, tubes were prepared containing 10 μL of TaqMan Fast Advanced Master Mix from Thermo Fisher Scientific, 5 μL of Milli-Q water, and 1 μL of the gene-specific assay (*C1QA* (Hs00381122_m1), *TMEM119* (Hs01938722_u1), *APOE* (Hs00171168_m1) or *CD68* (Hs04185218_g1)) per reaction. These solutions were then added to a MicroAmp Fast 96-well Reaction plate from Thermo Fisher Scientific. The cDNA samples were diluted with 180 μL of Milli-Q water, and 4 μL of each diluted sample was added to the appropriate wells. The plate was then sealed with plastic, centrifuged in an Axygen Mini Plate Spinner centrifuge, and placed in a PCR system (Quant Studio 3 from Thermo Fisher Scientific) to measure gene expression. The fold-change for each gene in each sample was then calculated using values of Actin beta (*ACTB*) as a blank reference. *ACTB* (Hs01060665_g1) is a gene that codes for one of six different actin proteins [40]. These proteins are highly conserved proteins that are involved in cell motility, structure, integrity, and intercellular signaling. Since *ACTB* is constitutively expressed in all cDNA samples, it was used as a reference gene. Its expression was subtracted during the calculations, allowing for analysis of only the gene expression of the target genes.

3.5 Phagocytosis assay

Another experiment conducted on the cell model was a phagocytosis assay. As previously written, healthy microglial cells function as macrophages, eliminating substances that could harm the CNS. However, when triggered by certain factors that impair their function, their ability to clear harmful substances may be reduced. This can be studied using a phagocytosis assay. The phagocytosis assay in this study uses E.Coli or Aβ labelled with a pH-dependent fluorescent dye to assess the ability of microglial cells to consume certain reagents while exposed to CSF from both healthy individuals and AD patients, alongside MiM serving as a standard control. pHrodo-E.Coli and pHrodo-$A\beta$ are non-fluorescent at neutral pH but become fluorescent in acidic environments, such as phagosomes inside the microglial cell. In that way, the uptake of bacteria by microglial cells can be measured, as consumed bacteria emit fluorescent light inside the microglial cells.

3.5.1 Optimization of pHrodo-E.Coli and pHrodo-$A\beta$oncentrations

The first step in the phagocytosis analysis was to test various concentrations of pHrodo-E.Coli and pHrodo-$A\beta$ to identify the concentration that produces the highest fluorescent signal while using the lowest amount of the reagent. Microglial cells were added to a 96-well plate, and after four days in culture, the experiment began. On the day of the experiment, four tubes containing 200 μL of MiM were prepared. 0, 1, 2.5, and 5 μL of pHrodo-E.Coli were then added to the tubes, respectively. 95 μL of the tubes were then added to the wells in duplicates (see Figure A3 in the appendix for plate layout). The cells were then incubated at 37°C for one hour, followed by fixation (see section 3.1.3). The fluorescence intensity was then measured using a plate reader with an excitation wavelength of 535 nm and an emission wavelength of 595 nm.

For the pHrodo-$A\beta$ experiment, microglial cells were added to a 96-well plate, and after four days in culture, the experiment began. Six tubes containing 200 μL of MiM were prepared. 0, 0.25, 0.5, 1, 2.5, and 5 μL of pHrodo-$A\beta$ were then added to the tubes, respectively. 50 μL of the tubes were then added to the wells in duplicates (see Figure A3 in the appendix for plate layout). The cells were then incubated at 37°C for 1.5 hours, followed by fixation (see section 3.1.3). The fluorescence intensity was then measured using a plate reader at the excitation wavelength of 535 nm and the emission wavelength of 595 nm.

3.5.2 Optimization of incubation time

Once the optimal concentrations of each reagent were determined, an experiment was conducted with pHrodo-E.Coli to investigate the effect of CSF on microglial phagocytic ability. To also consider the later effects of CSF, a 48-hour timepoint was included in the analysis. Similar to the first assay, microglial cells were added to a 96-well plate, and after four days in culture, the experiment began. 75 μL of MiM, AD-CSF, and CTRL-CSF were added to the cells 48 hours and 24 hours before the experiment (see plate layout in Figure A4 in the appendix). The CSF solutions were stored in the fridge (4°C) overnight. On the day of the experiment, 2.5 μL of pHrodo-E.Coli was added to each well, followed by an incubation at 37°C for 1 hour. The cells were then fixed, and the fluorescence intensity was read in a plate reader at the excitation wavelength of 535 nm and the emission wavelength of 595 nm.

3.5.3 Phagocytic activity assessment

Once the optimal incubation time was determined, experiments analyzing the impact of CSF on the microglial phagocytic ability began. For the pHrodo-E.Coli experiment, microglial cells were added to a 96-well plate, and after four days in culture, the experiment began. 70 μL of MiM, CTRL-CSF, and AD-CSF were added to the cells, followed by an incubation for 24 hours (see plate layout in Figure A5 in appendix). After 24 hours, 2.5 μL pHrodo-E.Coli was added to all test wells except the blank ones. The plate was incubated at 37°C for 1 hour. After incubation, the cells were fixed, and the fluorescence was measured in a plate reader with an excitation wavelength of 535 nm and an emission wavelength of 595 nm. The pHrodo-E.Coli experiment was repeated two times with a total of six replicates for each group.

For the pHrodo-$A\beta$ experiment, microglial cells were added to a 96-well plate, and after four days in culture, the experiment began. 70 μL of MiM, CTRL-CSF, and AD-CSF were added to the cells, followed by an incubation for 24 hours (see plate layout in Figure A5 in appendix). The pHrodo-$A\beta$ solution was prepared by other members of the research group, following a protocol provided by FUJIFILM Cellular Dynamics [41]. The resulting solution was a heterogeneous mixture containing $A\beta 42$ in various forms, including monomers, oligomers, and fibrils. After 24 hours, 0.55 μL of the pHrodo-$A\beta$ solution was added to all test wells except the blank ones. The plate was incubated at 37°C for 1.5 hours. After incubation, the fluorescence was measured in a plate reader with an excitation wavelength of 535 nm and an emission wavelength of 595 nm. The pHrodo-$A\beta$ experiment was repeated two times with a total of six replicates for each group.

An additional experiment was conducted for pHrodo-$A\beta$ to investigate whether the uptake of pHrodo-$A\beta$ was influenced by the presence of CSF or if the microglial cells were occupied absorbing other substances from the CSF (thereby decreasing their uptake of pHrodo-$A\beta$). Microglial cells cultured in a 96-well plate were cultured in 70 μL of MiM and CSF for 24 hours before the analysis (see Figure A6). The CSF and MiM were then removed and replaced with 70 μL of MiM before adding 0.55 μL of pHrodo-$A\beta$. The microglial cells were then incubated for 1.5 hours in an incubator (37°C) and then measured in a plate reader with an excitation wavelength of 535 nm and an emission wavelength of 595 nm. This experiment was repeated two times with a total of six replicates.

3.6 Methodology for analysis of microglial morphology

As previously stated, when microglial cells get triggered by external or internal stimuli, they adopt different types of states. These states can be characterized by differences in microglial morphology, which can be studied using confocal microscopy. For the morphology analysis, cocultures using cell line *WTSLi015-A* were prepared according to section 3.1.4. Additionally, one experiment was conducted creating cocultures with cells from the cell line (*CTRL1*). The cocultures were prepared similarly to those for the *WTSLi015-A* cell line. The cocultures were incubated in CoM, CTRL-CSF, and AD-CSF for 24 hours, fixated as described above, and stained to visualize microglia and neurons. The staining procedure is described below.

3.6.1 Immunocytochemistry assay

All antibodies mentioned in the conducted experiments were bought from BD Biosciences. Firstly, the cell cultures were washed three times for five minutes with Tris-buffered saline (TBS). Then the cells were permeabilized using permeabilization buffer (TBS + 0.3% Triton X-100) for 15 minutes at room temperature. After incubation, the cells were blocked using a blocking buffer (TBS + 0.3% Triton X-100 + 5% donkey serum) for one hour at room temperature. Later, the cells were incubated with primary antibody solution (primary antibody diluted with blocking buffer, 1:500) in the fridge overnight. For this, the primary antibodies ionized calcium-binding adaptor molecule 1 (Iba1) and anti-β-tubulin III (TUJ1) were used for staining the microglial cells and cortical neurons, respectively. After incubation, the cells were washed three times for five minutes with TBS.

The cells were then incubated with the secondary antibody solution (secondary antibody diluted with blocking buffer, 1:500) for one to two hours at room temperature in the dark. For the secondary antibodies, anti-rabbit was used for staining of the microglial cells, and anti-mouse was used for staining of the cortical neurons. The cells were then washed three times for five minutes with TBS. During the second wash step, DAPI diluted in TBS (1:1000) was used for staining cell nuclei. The cells were then washed with MilliQ water. Once the assay was finished, the coverslips were removed from the wells and placed on glass slides using ProLong Gold antifade mounting media.

3.6.2 Confocal Microscopy

Confocal microscopy enables high-resolution imaging by using a laser that is reflected by a dichromatic mirror and focused on the sample via the objective lens (see image *A* in Figure 6) [42]. The laser beam scans the sample point by point to generate an image. The emitted fluorescence from the sample travels back through the same optical path and is detected after passing through a pinhole, which blocks out-of-focus light. This selective detection enhances optical sectioning and allows for 3D reconstruction of the sample from sequential image slices, known as a z-stack. The pinhole size can be adjusted to control the optical section thickness and signal intensity.

3.6.3 Morphology analysis

After staining, the cells were imaged using the confocal microscope, followed by an analysis in ImageJ and RStudio. The methodology is described below.

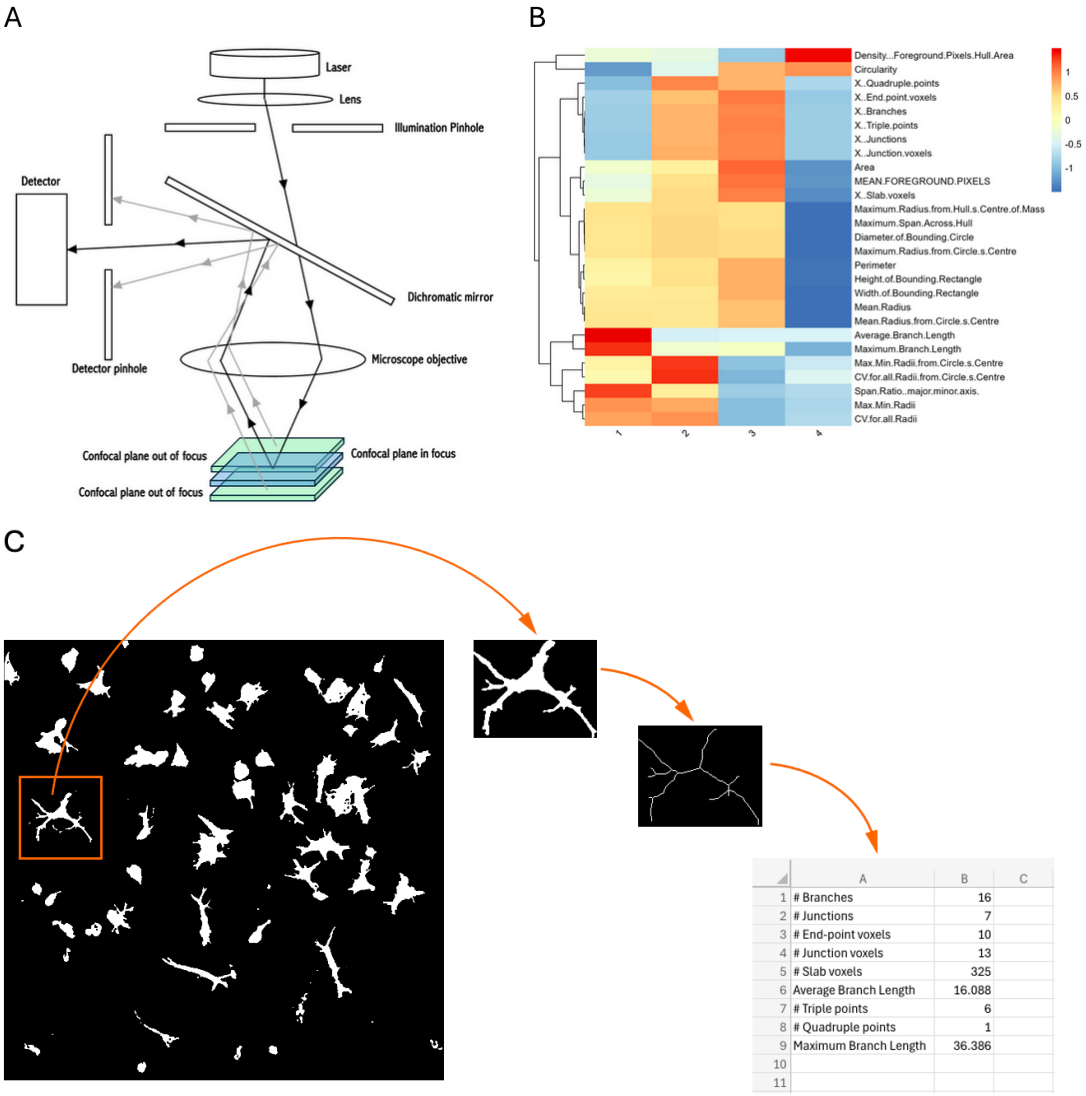

Figure 6: ***A)*** A simplified illustration of a confocal microscope. ***B)*** An example of a heatmap generated from the RStudio pipeline for microglia morphology analysis, visualizing all the morphology parameters for each cluster. ***C)*** The methodology of the ImageJ pipeline. Firstly, each microglial cell in the images was isolated and analyzed as a single-cell image. For each cell, a corresponding skeleton image was generated to measure morphological parameters such as branch length and junctions. All data were then saved in an Excel file.

3.6.4 ImageJ

Z-stack images of both cocultures and monocultures (containing only microglial cells) were captured using confocal microscopy and saved as 16-bit TIFF files. Additional information on the confocal microscope settings is provided in Appendix A1. The three fluorescence channels were merged, and a maximum intensity projection was applied to generate 2D pictures for further analysis. All image processing was performed using *ImageJ* (ImageJ version 2.16.0/1.54p with Java 1.8.0_322). To analyze microglial morphology, a published pipeline by Kim et al. [43] was followed using ImageJ and Rstudio.

First, the channels representing neurons and cell nuclei were removed, leaving single-channel images containing only microglial cells. Size filtering was performed using the BioVoxxel plugin to exclude noise outside the threshold range defined by the pipeline. This was followed by the MicrogliaMorphology Program plugin, which isolated individual microglial cells and generated skeletonized images to measure parameters such as branch length, number of junctions, and size (see image *C* in Figure 6). Additional complexity analysis was performed using the FracLac plugin. All extracted morphological data were exported as Excel files, along with skeleton images and other output files. These files were then used as input for further analysis in RStudio. The full ImageJ and RStudio pipeline, including all custom scripts, is accessible via a GitHub repository [37].

3.6.5 RStudio

The morphology analysis continued in *RStudio* (RStudio version: 2024.12.1 + 563), using the plugin *MicrogliaMorphologyR* from the pipeline mentioned in the section above. Morphological data obtained from the ImageJ analysis were first imported and merged into a single large matrix containing parameter values for each microglial cell across all images and experimental groups. This matrix was used to generate a heatmap showing feature correlations, with thresholds set at Pearson's $r > 0.8$ and $p < 0.05$. The pipeline also produced boxplots and density plots illustrating the distribution of morphological parameters across all conditions.

Next, the data was normalized. Three normalization strategies were tested: log transformation, min-max scaling, and z-scoring. For the principal component analysis (PCA), the log-transformed dataset was selected as the most appropriate. PCA was then performed to assess correlations between morphological features across different sample groups. To identify distinct microglial morphology states, k-means clustering was applied to the PCA-transformed data. The optimal number of clusters was determined using the within-cluster sum of squares (WSS) method and silhouette analysis. Cluster data containing all morphological parameters were visualized in a heatmap (see image *B* in Figure 6). Based on the cluster-specific parameter values, each cluster was interpreted as representing a specific microglial morphology. The pipeline also generated boxplots displaying the proportion of each morphology across the different sample groups.

Finally, statistical analysis were performed to evaluate differences in cluster proportions and individual morphological parameters. Posthoc comparisons were carried out using Bonferroni correction, and model assumptions were tested using QQ plots and the Shapiro–Wilk test. Statistically significant features ($p < 0.05$) were visualized using bar plots displaying $-\log_{10}(p)$ values.

4 Results

Below, the results from the functional assays, qPCR, and morphology analysis are presented. First, the findings from the cell model validation are shown, followed by the results from the analysis of the CSF pools. Next, the qPCR data are presented, followed by the phagocytosis results. Finally, the outcomes of the morphology analysis are presented. All diagrams were created using GraphPad (Prism 10), where statistical tests such as the Kruskal–Wallis test and two-way ANOVA were performed on the datasets to identify significant changes. Additionally, outliers were removed using a ROUT (1% and 5%) test in GraphPad. Statistical analysis was also preformed on the morphology analysis results using Rstudio. This can be found in section 4.5.1.

4.1 Validation of the cell model

A cell viability assay, cytotoxicity assay, and a staining for cell division were conducted to validate the cell model. The results from these experiments can be found in Figure 7 below.

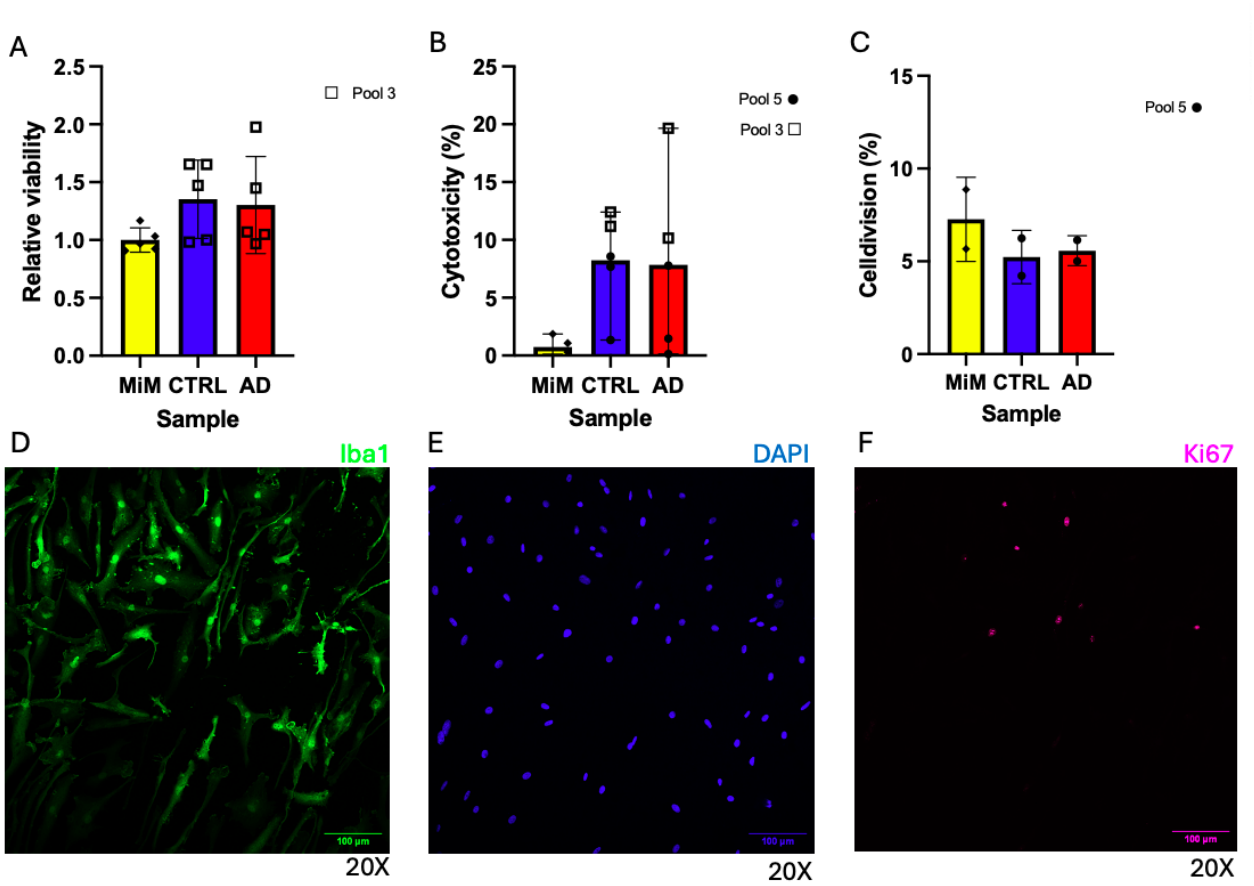

Figure 7: ***A***) Measured relative viability of the microglial cells when cultured in MiM, CTRL-CSF, and AD-CSF for 24 hours. MiM as a reference. ***B***) Calculated cytotoxicity (%) of the microglial cells when cultured in MiM, CTRL-CSF, and AD-CSF for 24 hours. MiM as a reference. ***C***) The average percentage of cell division per sample in microglial cell cultures after 24 hours of incubation under MiM, CTRL-CSF, and AD-CSF conditions. Each point represents the average percentage of dividing cells in each well after 24 hours of culture in MiM, CTRL-CSF, and AD-CSF conditions. MiM as a reference. ***D***) A single-channel confocal image of Iba1-stained microglial cells cultured in MiM for 24 hours. ***E***) A single-channel confocal image of DAPI-stained cell nuclei of microglial cells cultured in MiM for 24 hours. ***F***) A single-channel confocal image of Ki67-stained microglial cell nuclei undergoing cell division after 24 hours in culture in MiM.

Plot *A* in Figure 7 shows a slight non-significant increase in cell viability in the CTRL-CSF and AD-CSF groups compared to the MiM-group. Plot *B* shows an increase in cytotoxicity in the CTRL-CSF and AD-CSF groups compared to the MiM group, where the AD-CSF group has the highest cytotoxicity. Plot *C* shows an increase in cell division in the MiM group compared with the CTRL- and AD-groups, where AD has the lowest cell division percentage. Image *F* in Figure 7 shows cell nuclei undergoing division in a monoculture with microglial cells cultured in MiM.

4.2 Analysis of the CSF pools

To investigate differences in protein expression between AD- and CTRL-pools, differential expression analysis was conducted using data generated from a NULISA analysis. Proteins with more than 50% zero values were excluded to ensure data quality.

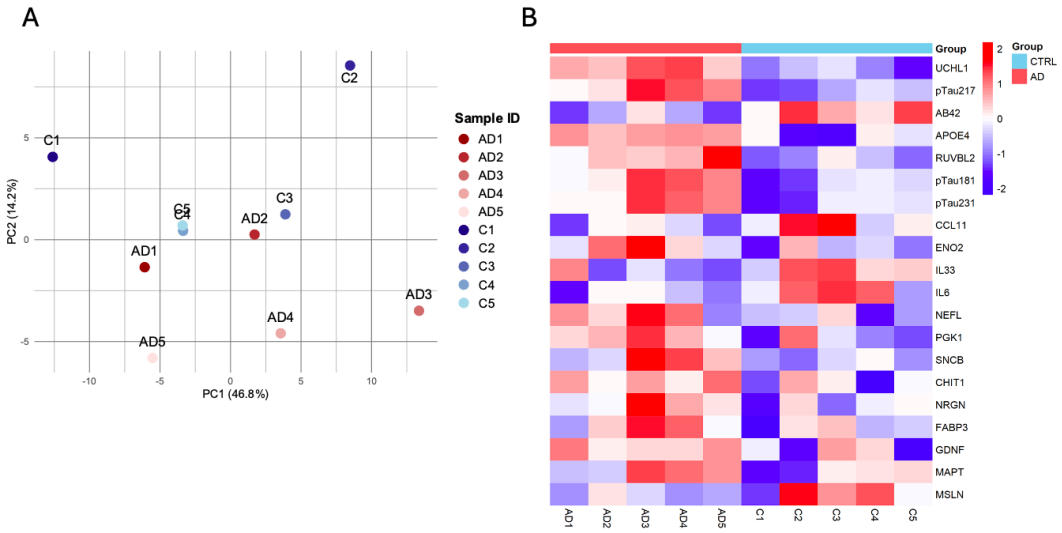

Figure 8: ***A)*** PCA plot showing the distribution of CSF pools from AD- and CTRL-groups based on global protein expression. Samples from the AD- and CTRL-groups show partial separation along PC1 (46.8% variance explained) and PC2 (14.2% variance explained). ***B)*** Heatmap of the top 20 proteins showing the greatest difference in relative abundance between the AD- and CTRL-CSF groups using FDR-adjusted p-values. Rows represent proteins, and columns represent CSF pools. The colors represent the relative abundance.

A principal component analysis (PCA) was performed to assess the overall separation of the ten pooled samples (five AD and five CTRL) based on protein expression profiles. As shown in Figure 8, plot A, the PCA revealed a partial separation between the AD and CTRL samples along the first principal component (PC1), which accounted for 46.8% of the total variance. This showcased the variation within the groups, particularly between CTRL-CSF pools 1 and 2, and AD-CSF pools 1 and 3. The PC2, which accounted for 14.2% of the total variance, instead highlighted the differences between the pools. To identify specific proteins that were significantly altered between groups, a linear model was fitted for each protein, followed by p-value adjustment using the Benjamini-Hochberg FDR method. The top 20 proteins with the highest difference in protein abundance between CTRL-CSF and AD-CSF, according to the p-values, were visualized in a heatmap (Figure 8, plot *B*), which displays clear differences between AD and CTRL pools.

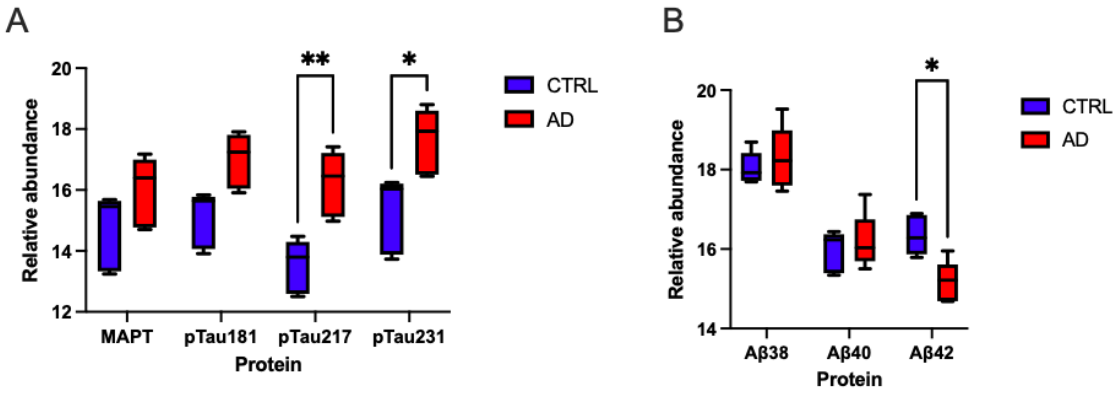

Figure 9: ***A***) The relative abundance of MAPT, pTau181, pTau217, and pTau231 in the AD- and CTRL-CSF groups. ***B***) The relative abundance of $A\beta 38$, $A\beta 40$ and $A\beta 42$ in the AD- and CTRL-CSF groups.

Tau-related proteins (MAPT, pTau181, pTau217, and pTau231) were examined in greater detail (see plot A in Figure 9). Among these, pTau217 and pTau231 show a significant increase in AD-CSF compared to CTRL-CSF, while a clear but non-significant increase for pTau181 can be observed. Similarly, MAPT is elevated in AD-CSF, but this difference does not reach significance. Amyloid-beta isoforms were also analyzed (see plot B in Figure 9). Notably, $A\beta 42$ levels were significantly higher in CTRL-CSF compared to AD-CSF. $A\beta 42$ was also among the top 20 differentially expressed proteins in the global analysis (see plot B in Figure 8). The $A\beta 38$ and $A\beta 40$ shows a higher abundance in both the AD-CSF and CTRL-CSF compared to $A\beta 42$. However, they do not show any significant difference in abundance between the AD- and CTRL-CSF.

4.3 qPCR

To investigate the gene expression of *APOE*, *TMEM119*, *C1QA*, and *CD68* in microglial cell cultures cultured in MiM, CTRL-CSF, and AD-CSF, a qPCR was conducted. The results from this can be seen in Figure 10 below.

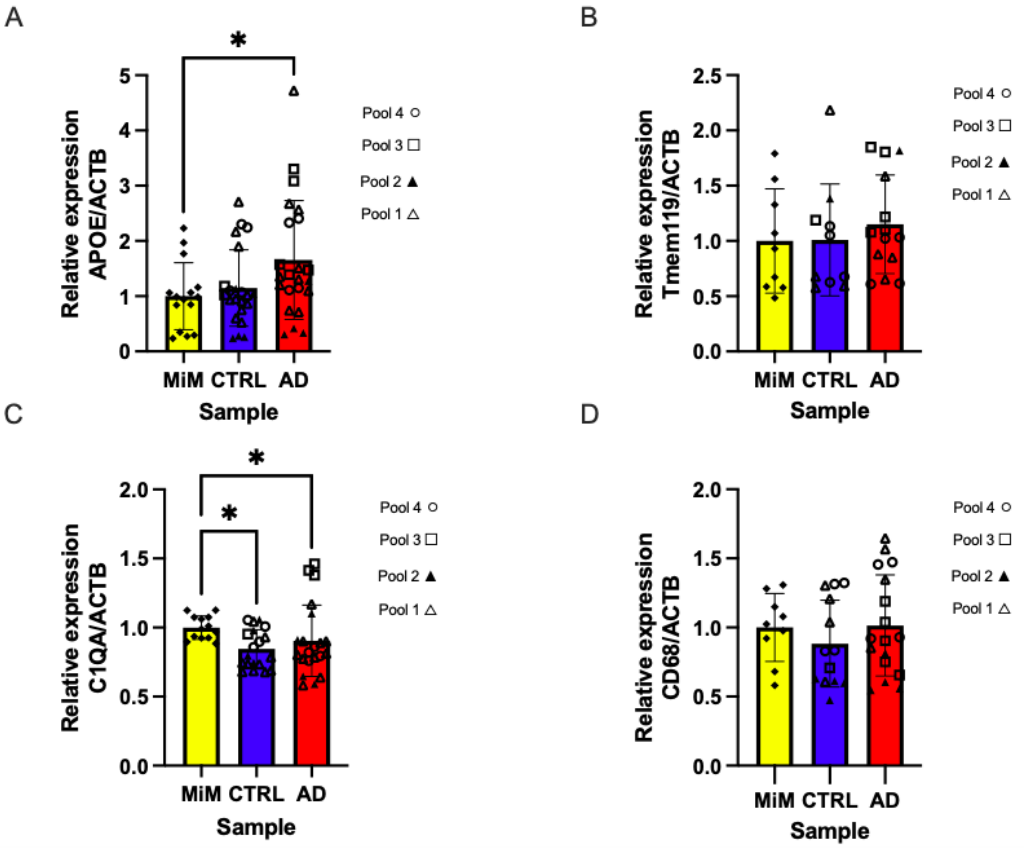

Figure 10: ***A***) Relative *APOE* expression in the microglial cells when cultured in MiM, CTRL-CSF, and AD-CSF for 24 hours. ***B***) Relative *TMEM119* expression in the microglial cells when cultured in MiM, CTRL-CSF, and AD-CSF for 24 hours. ***C***) Relative *C1QA* expression in the microglial cells when cultured in MiM, CTRL-CSF, and AD-CSF for 24 hours. ***D***) Relative *CD68* expression in the microglial cells when cultured in MiM, CTRL-CSF, and AD-CSF for 24 hours.

Plot *A* in Figure 10 shows a significant increase in *APOE* gene expression in the AD-CSF group compared to the MiM and CTRL-CSF groups. Plot *B* does not show a significant change in *TMEM119* gene expression in the CSF groups compared to MiM, although a slight increase is observed. Plot *C* shows no significant change in *C1QA* gene expression. However, it shows a slight increase in the AD-group. Plot *D* indicates a slight increase in gene expression in the AD-CSF group compared to the MiM and CTRL-CSF groups.

4.4 Phagocytosis assay

The observed increase in the phagocytosis-associated gene *CD68* in the qPCR results prompted further investigation into the phagocytic capacity of the microglial cells. The results from all phagocytosis assays can be seen in Figure 11 below.

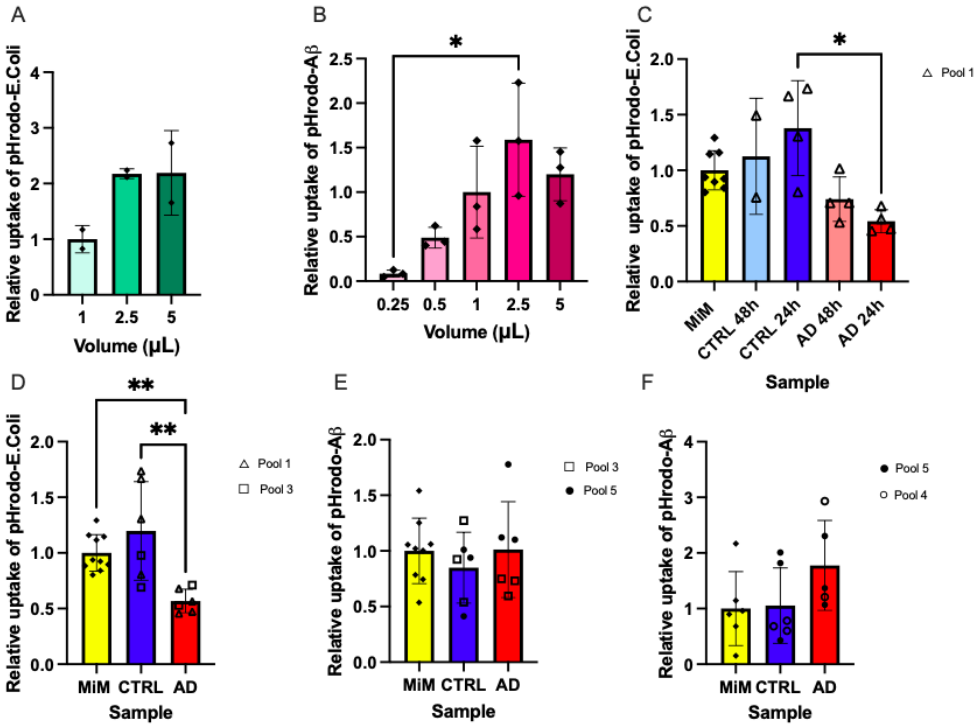

Figure 11: ***A***) Microglia relative uptake of pHrodo-E.Coli in μL in relation to its volume. 1 μL as a reference. ***B***) Microglia relative uptake of pHrodo-$A\beta$ in μL in relation to its volume. 1 μL as a reference. ***C***) Uptake of pHrodo-E.Coli for microglial cells cultured in CSF for 48 hours and 24 hours in CSF. MiM as a reference. ***D***) Uptake of pHrodo-E.Coli for microglial cells cultured in MiM, CTRL-CSF, and AD-CSF for 24 hours. MiM as a reference. ***E***) Uptake of pHrodo-$A\beta$ for microglial cells cultured in MiM, CTRL-CSF, and AD-CSF for 24 hours. MiM as a reference. ***F***) Uptake of pHrodo-$A\beta$ for microglial cells cultured for 24 hours in MiM, CTRL-CSF, and AD-CSF, followed by the removal of these media and replacement with MiM before adding pHrodo-$A\beta$. MiM as a reference.

The results from plots A and B in Figure 11 showed that a volume of $2.5\mu L$ and a volume of $0.55\mu L$ for pHrodo-E. coli and pHrodo-$A\beta$, respectively, showed the highest uptake for their volume. Therefore, these volumes were used consistently in further experimentation. To also consider the later effects of CSF, a 48h timepoint was included in the analysis. The results from this experiment are shown in plot C and show a significant decrease in uptake of pHrodo-E.Coli in the AD-CSF group when cultured in CSF for 24 hours. Therefore, for the following experiments, a 24-hour incubation was used. Plots D and E in Figure 11 show the effect on the phagocytic ability of the microglial cells in MiM, CTRL-CSF, and AD-CSF for 24 hours before adding pHrodo-$A\beta$ and pHrodo-E.Coli. Plot D shows a significant decrease in phagocytic ability between the MiM and AD-group, and between the CTRL and AD-group. Plot E does not show a significant decrease between any of the three groups. However, the phagocytic ability is slightly lower in the CTRL-group compared to the MiM and AD-groups. Plot F in Figure 11 shows an increase in phagocytic ability for the AD-group compared to the CTRL and MiM groups after CSF priming, where the CSF and MiM were replaced with fresh MiM after 24 hours.

4.5 Morphology analysis

In total, four coculture experiments were performed, analyzing 2,614 microglial cells in the AD group, 2,640 cells in the CTRL group, and 3,008 cells in the CoM group. Representative images from one of these experiments are shown in plots $A-C$ in Figure 12. On average, 64 microglial cells were analyzed per image. Plots D and E in Figure 12 present the combined results from these four experiments. One additional morphology analysis was performed on a coculture using cells from a second cell line (*CTRL1*), while another analysis was conducted using a monoculture containing only microglial cells from the cell line *WTSLi015-A*. The results from these experiments are presented in plots A–E in Figure A7 and A8 in the appendix. A comparison between the monoculture experiment and coculture experiment (cell line *WTSLi015-A*) can be seen in Figure 13.

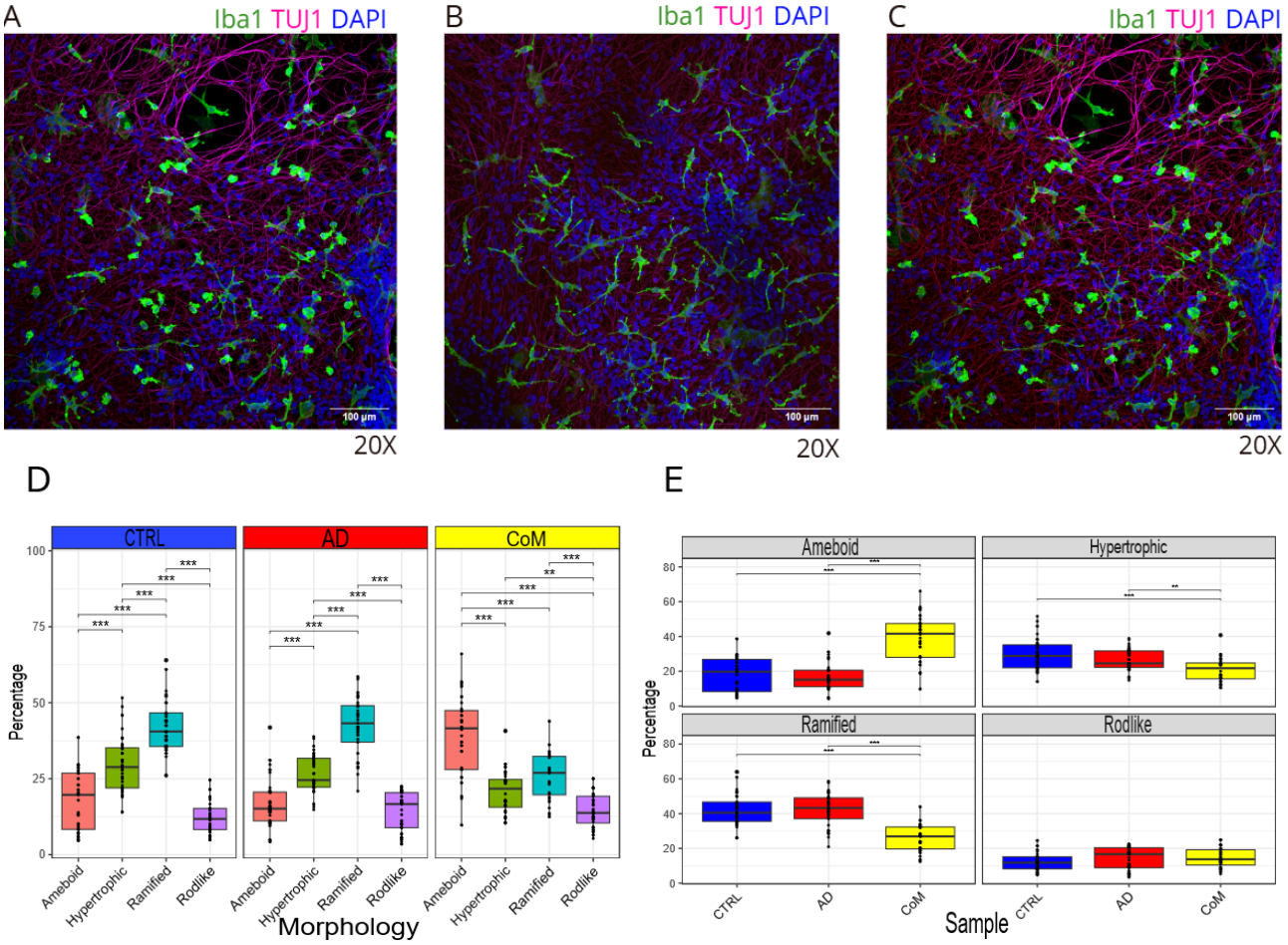

Figure 12: **A – C)** Three-channeled images of a coculture containing cortical neurons and microglial cells cultured in CoM, CTRL-CSF, and AD-CSF, respectively, for 24 hours. Iba1 was used to stain microglial cells, TUJ1 to stain cortical neurons, and DAPI to stain cell nuclei. **D–E)** The distribution of different microglial morphologies within and between the sample groups, where asterisks indicate statistically significant differences ($p < 0.05 = *$, $p < 0.01 = **$, $p < 0.001 = ***$). The statistical significance was calculated using linear mixed models with fixed effects.

Images *A*, *B*, and *C* in Figure 12 show representative confocal images from one of the morphology experiments, where cocultures containing microglial cells and cortical neurons cultured in CSF for 24 hours. The images show a clear difference in microglial morphology between the cocultures cultured in CoM (image *A*) compared to those cultured in CSF (image *B* and *C*). The CoM group displays microglial cells with a more rounded (ameboid) morphology, whereas the CSF groups exhibit microglial cells with a more hypertrophic or ramified morphology.

Plots *D* and *E* in Figure 12 summarize the morphological distribution of microglia across the three conditions (CoM, CTRL-CSF, and AD-CSF). Plot *D* shows the proportions of each morphology type (ameboid, hypertrophic, ramified, and rodlike) within each group. Furthermore, plot *E* compares the distribution of each morphology between the treatment groups. Plot *E* shows significant differences between CoM and the CSF-treated conditions for multiple morphologies, while no significant differences were detected between the AD- and CTRL-groups. Plot *D* shows that the AD- and CTRL-CSF groups have a similar distribution of the four morphologies, where the highest percentage of microglial cells exhibited a ramified morphology, followed by hypertrophic, amoeboid, and, lastly, rodlike morphology. The CoM-group shows a higher percentage of microglial cells with an ameboid morphology compared to the CTRL- and AD-group. Furthermore, no significant differences were observed between the three conditions for the rodlike morphology (see plot *E*).

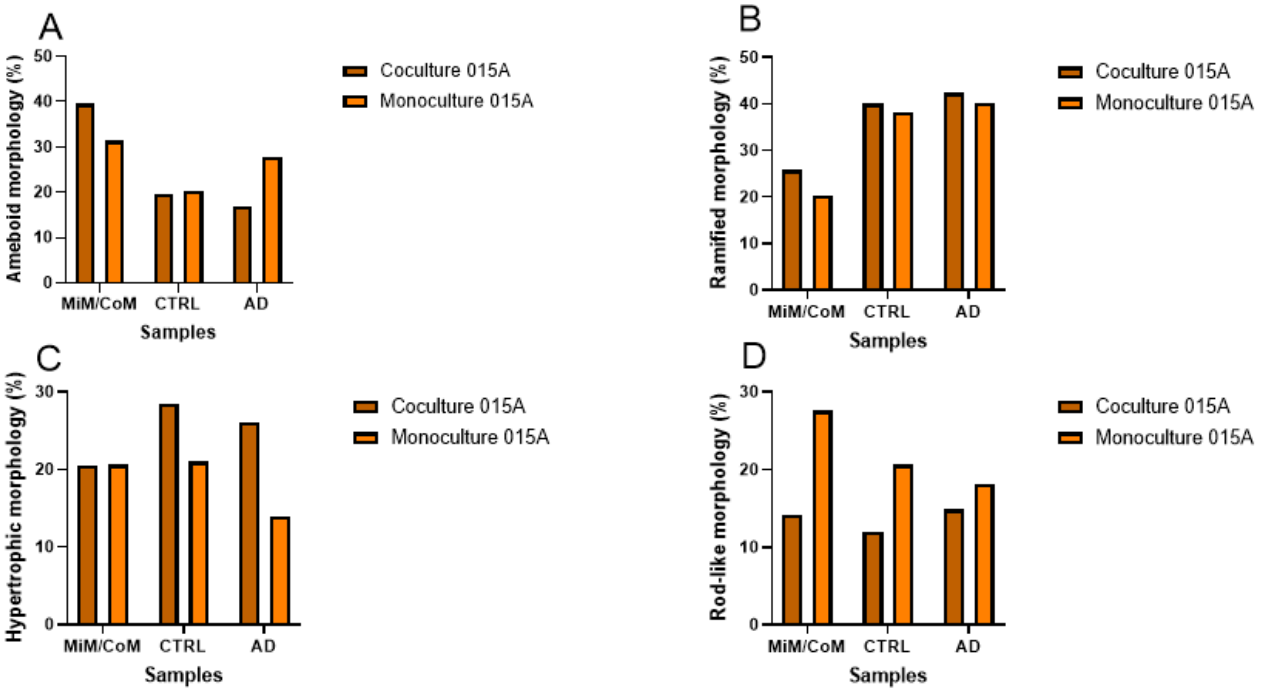

Figure 13: The percentage of microglial cells exhibiting different morphologies in both a coculture with cortical neurons and a monoculture of microglial cells, after being cultured for 24 hours under three different conditions: MiM/CoM, CTRL-CSF, and AD-CSF. All cells were derived from cell line WTSLi015-A. ***A)*** Amoeboid morphology. ***B)*** Ramified morphology. ***C)*** Hypertrophic morphology. ***D)*** Rodlike morphology.

Figure 13 illustrates the distribution of the different microglia morphologies between the cocultures containing cortical neurons and microglia, and the monocultures containing only microglia. Additional plots showing the morphology distribution of the monocultures can be found in the appendix in Figure A8. In Figure 13, it is possible to see that while the cocultures and monocultures show quite similar results, there are some notable differences between them. The monoculture showed approximately double the proportion of rodlike cells compared to the

coculture under the same conditions (see plot D). Additionally, plot A shows that about 10 % more amoeboid cells were detected in the coculture than in the monoculture when cultured in CoM/MiM. In plot C the AD-CSF monoculture showed roughly half the proportion of hypertrophic cells compared to the coculture. While in plot B, there were no pronounced differences in microglial morphology between the coculture and the monoculture.

4.5.1 Statistical analysis of morphology results

Statistical comparisons between the three conditions (CoM, AD-, and CTRL-CSF) were performed using linear mixed models with fixed effects for condition and morphology. The mixed model was chosen to account for repeated images within samples, where image ID was included as a random effect. Posthoc comparisons were corrected for multiple testing using a Bonferroni adjustment. To assess whether the mixed model was an appropriate fit for the data, residual diagnostics were performed using the DHARMa package in RStudio, which simulates standardized residuals from the fitted model to test for deviations from expected behavior. The QQ-plot and the residuals vs. predicted values plot are shown in Figure 14.

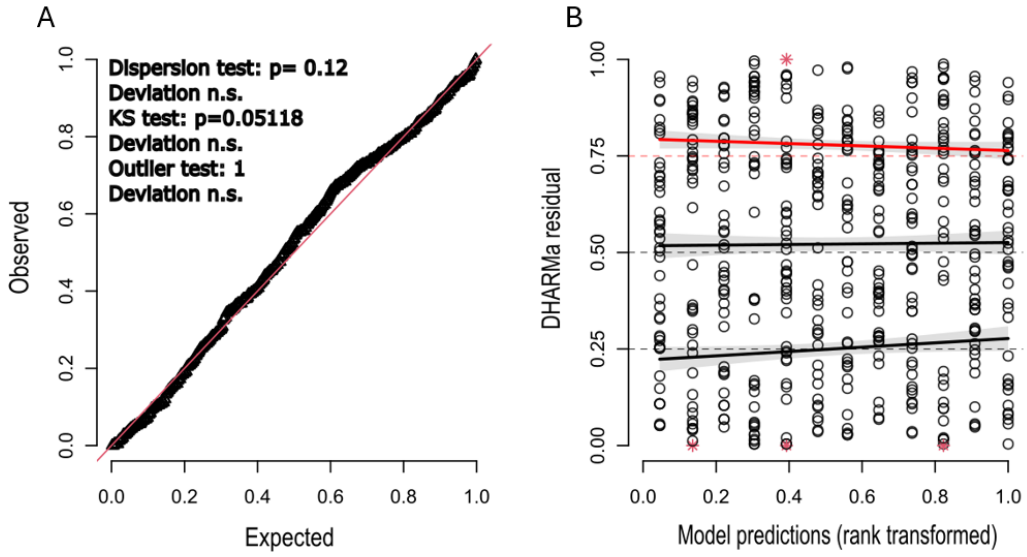

Figure 14: **A)** QQ-plot of scaled DHARMa residuals from the mixed model assessing microglial morphologies for coculture *WTSLi015-A*. The Kolmogorov–Smirnov test for uniformity, dispersion test, and outlier test were all non-significant, suggesting no major violations of model assumptions. **B)** Residuals versus predicted values for coculture *WTSLi015-A*, showing a minor deviation at the 0.75 quantile (red line), though the overall quantile test was non-significant, supporting model validity.

The QQ-plot (Figure 14 plot A) compares the distribution of the simulated residuals to a theoretical uniform distribution [44]. If the model fits the data well, the points should fall along the diagonal line. Deviations from this line may suggest issues, such as non-uniformity, skewness, or model misspecification. DHARMa also includes statistical tests which are summarized in the plot, where the Kolmogorov-Smirnov test for uniformity (non-significant even though it was close to being significant with $p = 0.05118$) checks whether the residuals follow a uniform distribution, the dispersion test ($p = 0.12$) detects whether the variance in residuals is too high or too low, and an outlier test ($p = 1$) checks whether any extreme values behave unusually. In this case, all three tests were non-significant, which suggests that the model residuals behave as expected, although the Kolmogorov–Smirnov test was close to the significance threshold. This supports that the residuals follow an approximately uniform distribution and that the model fits the data.

Plot *B* in the same figure displays residuals on the y-axis and the predicted values from the model on the x-axis. Ideally, the residuals should appear randomly scattered without any patterns, indicating equal variance and no systematic bias [44]. The lines in the plot show quantile bands, which help visualize whether residuals fall within expected ranges. If residuals cluster outside these bands or show a curve, this may suggest model issues. A slight deviation is seen around the upper quantile (0.75), but the combined quantile test was non-significant.

5 Discussion

Below are the results from the evaluation of the cell model, the analysis of the CSF pools, the qPCR, phagocytosis assay, and morphology analysis discussed.

5.1 Validation of the cell model

The results from the cell viability assay showed no significant change in viability between MiM, CTRL-, and AD-CSF. This specific assay is based on the metabolic activity of the cells. The results showed a slightly increased metabolic activity in microglial cells cultured in CSF compared to those cultured in MiM (see Figure 7). This may suggest that the cells are more stimulated in the CSF environment, leading to an increased metabolism and therefore showing a higher absorbance, which is related to viability in this assay.

The cytotoxicity assay did not show any significant differences between the three groups, although higher levels of cell damage were observed in microglial cells exposed to CTRL-CSF and AD-CSF. However, near the end of the project, it was discovered that CSF itself may contain LDH [45]. Since the assay measures total LDH concentration, the results reflect both LDH present in the CSF and LDH released from the damaged or dying cells in the cell culture. As a result, no definitive conclusions can be drawn from these findings, and further experiments are needed to accurately assess cytotoxicity in microglial cells cultured in CSF. Finally, the Ki67 staining showed no significant changes in the proliferation for the microglial cells cultured under the three conditions: MiM, CTRL-CSF, and AD-CSF (see plot *C* in Figure 7). As microglial cells in the human brain rarely divide [20], this low proliferation rate supports the relevance of the model, indicating that it more closely reflects the behavior of microglia in vivo.

To summarize the results from all functional assays conducted to validate the cell model, there were no significant decreases in cell viability or cell division. Based on these findings, the model was deemed suitable for further studies of microglial cells.

5.2 Analysis of the CSF pools

The PCA of the NULISA data (see Figure 8) showed a separation between the CTRL-CSF and AD-group. Plot *A* in Figure 9 highlights clear differences in the relative abundance of AD-related proteins. Specifically, tau proteins showed to be elevated in AD CSF compared to CTRL-CSF. This was expected as one of the hallmarks of AD is the accumulation of tau tangles, which contributes to the increased tau levels in AD-CSF (see section 1.1).

The differences in relative abundance of $A\beta$ between the two groups were less noticeable (see plot *B* in Figure 9). However, there is a difference in relative abundance between the CTRL-CSF and AD-CSF for $A\beta42$, where CTRL-CSF has a higher abundance of $A\beta42$. As previously written in section 1, $A\beta42$ is one of the $A\beta$ isoforms with the highest tendency to aggregate. In AD, $A\beta42$ tends to form aggregates and accumulate in the brain, leading to a reduced relative abundance of soluble $A\beta42$ in the CSF [46]. In contrast, in CTRL-CSF, $A\beta42$ is not aggregated to the same extent, resulting in higher detectable levels. Therefore, it is expected that the concentration of $A\beta42$ would be higher in CTRL-CSF compared to AD-CSF. $A\beta38$ and $A\beta40$ show higher relative abundance compared to $A\beta42$, likely for the same reason as mentioned above, $A\beta42$ has a higher tendency to aggregate than the other two isoforms. As a result, there is a higher abundance of soluble $A\beta38$ and $A\beta40$ in the CSF, and the difference in their relative abundance between CSF-groups is not as pronounced as it is for $A\beta42$.

Even though the CSF-groups are noticeably separated, as shown in plot *A* in Figure 8, the PCA plot also displays variability within each group, with apparent differences between individual CSF pools. An explanation for this could be that the levels of different types of biomarkers in AD-CSF may vary from person to person, depending on other health conditions the patient may have [47]. For example, conditions such as chronic kidney disease, body mass index (BMI), and diabetes have been shown to affect the levels of specific biomarkers in the CSF [47]. Since each pool consists of CSF samples from five different patients, a variation is expected and likely reflects the natural variability between individual patient samples [34].

However, the separation within each group is less desirable, as it may lead to inconsistent effects on the microglial cells and complicate the interpretation of the results. Given the clear separation between the CTRL- and AD-groups (see plot *A* in Figure 8), the CSF can be used for further experimentation since differences in microglial cell responses between the two groups should be detectable.

To summarize the results regarding the CSF pools, different pools were used throughout the experiments, which strengthens the reliability of the results and make the findings more robust. However, the variation between the CSF pools should still be taken into account when interpreting the findings, as different CSF pools may affect the microglial cells in different ways.

5.3 qPCR

The results from the qPCR showed a significant increase in the relative expression of *APOE* in the AD-CSF compared to MiM (see plot *A* in Figure 10). *C1QA* expression was significantly lower in the CTRL-CSF and AD-group compared to MiM (see plot *C* in the same figure). However, there was a slight increase in expression for the AD-group compared to the CTRL-group. Since both *C1QA* and *APOE* are genes known to be upregulated during neuroinflammation (see section 1.2), an increase in their expression in the AD-CSF compared to CTRL-CSF is expected and reflected in the results.

The *TMEM119* gene did not show any significant differences in gene expression between the three groups, though it showed a slightly higher expression in the AD-group compared to MiM and CTRL-CSF (see plot *B* in Figure 10). The *TMEM119* gene is a microglia-specific marker that has been seen to be upregulated during microglia activation [21]. Based on this, it was expected that *TMEM119* expression would be lower in the CTRL-group compared to the AD-group.

The expression of *CD68* does not show any significant change in gene expression between the three groups (see plot *D* in Figure 10). However, the gene expression is slightly higher in the AD-group compared to the CTRL-group. *CD68* is a phagocytic marker gene that becomes upregulated when microglial cells are exposed to different types of stimuli (see section 1.2). Therefore, an increased expression of *CD68* in the AD-group compared to the CTRL-group is expected. To summarize the results for the qPCR, all genes tested were shown to have an increase in expression for the AD-group compared to the CTRL-group.

5.4 Phagocytosis assay

For the phagocytosis assay, as well as all other experiments conducted in this study, the cell cultures were incubated in CSF for 24 hours. This decision was based on the results shown in plot *C* of Figure 11, where a clear effect was observed after 24 hours. Additionally, previous studies have reported similar incubation times, including the exposure of microglial cells to brain-derived factors for 24 hours and organoids to CSF for the same duration, which further supports our choice [48, 49].

The slight increase in *CD68* gene expression in the AD-group indicates an increased phagocytic activity in microglial cells under that condition. This is supported by the results from the $A\beta$ phagocytosis assay (see plots *E* and *F* in Figure 11). While neither plot shows a significant increase in $A\beta$ uptake, both display a slightly higher uptake in the AD-group. This suggests that microglial cells cultured in AD-CSF may be in a more activated state, which could explain the increased phagocytic activity.

Furthermore, the higher $A\beta$ uptake observed in plot *F* (CSF priming) compared to plot *E* indicates that removing the CSF before adding pHrodo-$A\beta$ increases uptake. One possible explanation for this could be that when CSF is left on the cells during the assay (as in plot *E*), the microglia may be occupied with absorbing various substances already present in the CSF, which could compete with the pHrodo-$A\beta$ for uptake. In contrast, in the CSF priming condition (plot *F*), where the CSF is replaced with MiM before adding pHrodo-$A\beta$, there is less competition, allowing more efficient uptake. This may also explain the phagocytosis results for pHrodo-E.Coli (see plot *D* in Figure 11). The plot shows a significant decrease in phagocytic uptake of pHrodo-E.Coli in the AD-group compared to both the CTRL-group and the MiM-group. This reduced uptake could be due to the same reason mentioned previously, that the microglial cells are occupied with absorbing other substances present in the CSF. Due to the limited availability of CSF, an additional experiment investigating CSF priming for pHrodo-E.Coli could not be conducted.

5.5 Morphology analysis

The most pronounced morphological differences were observed between the CSF-treated and CoM-treated groups, with significant differences found between the CoM condition and both CSF groups across all morphological categories, except for the rodlike morphology (see plot *E* in Figure 12). The most unexpected result in the morphology analysis was that cocultures incubated in CoM displayed a significantly higher proportion of microglial cells with an amoeboid morphology compared to the CSF-treated groups. As previously mentioned, an amoeboid morphology is associated with increased phagocytic activity in microglial cells [24]. It is therefore surprising that CoM, the coculture medium used to grow cocultures, induces highly activated microglia. One possible explanation for this could be that neurons in the CoM condition are negatively affected, either due to the composition of the medium or stress caused by coculturing with microglial cells, which may lead to neuronal damage or death. This could trigger microglial activation and increase phagocytic behavior to clear dying neurons. Such a response is consistent with the role of microglia in the brain, where they are known to engulf damaged or dead neurons [16].

In contrast, microglia in the CSF-treated groups exhibited a higher proportion of ramified and hypertrophic morphologies and relatively few amoeboid cells. This might indicate that the CSF provides a more supportive environment for neurons, potentially due to the presence of neurotrophic factors or other nutrients that enhance neuronal survival. A previous study has demonstrated that culturing neurons in human CSF increased synapse formation and promoted the development of neural circuits [50]. This could explain the more ramified and hypertrophic microglia morphologies observed in the CSF-treated groups (see plot *D* in Figure 12) as fewer dead or damaged neurons would be triggering microglial phagocytosis. Furthermore, the microglial cells showed a relatively high percentage of hypertrophic morphology in both AD- and CTRL-CSF conditions (see plot *D* in Figure 8). Hypertrophic morphology is often associated with a reactive but less phagocytic state than the ameboid state (see section 1.2.1). This suggests that microglial cells might sense changes in their environment but respond in a way that does not necessarily result in increased phagocytic activity or adoption of an amoeboid form.

No significant morphological differences were observed between the two CSF groups. This was unexpected, given that the NULISA results (see PCA plot *A* in Figure 8) showed a clear separation between AD-CSF and CTRL-CSF. As previously mentioned, microglial cells transition into a DAM state during disease progression (see section 1.2). Therefore, one would expect to observe differences in microglial morphology between the CTRL- and AD-group. One possible explanation is that the concentration of soluble Aβ42 is lower in AD-CSF compared to CTRL-CSF, which could lead to a similar level of microglial activation in both conditions. In CTRL-CSF, soluble Aβ42 may contribute to microglial activation, while in AD-CSF, other components such as proinflammatory cytokines and tau proteins might play a more prominent role in activating the microglial cells. Alternatively, microglial cells might respond more strongly to Aβ plaques than to soluble Aβ42. As a result, the microglia in the AD-CSF cultures may not be as activated as they would be in the brain of an AD patient, where the concentration of Aβ plaques is significantly higher. Another possible explanation for the results could be the duration of CSF incubation. Studies have shown that microglial cells rapidly transition between different morphological states in response to external stimuli [51]. For instance, one study demonstrated that microglia can rapidly change state and migrate at speeds of up to 1.25 μm/min toward a site of CNS injury [52]. This suggests that a 24-hour incubation period may be too long for accurate morphology analysis. Microglial cells may initially alter their morphology upon CSF stimulation but then revert to a ramified state once the stimulus has been processed. The cells might return to a more ramified state before the 24 hours are over, which could make it hard to detect differences in morphology.

The morphology analysis was also performed on a monoculture containing only microglial cells (see Figure A8 in the appendix). Comparative plots illustrating the distribution of the four microglial morphologies between monoculture and coculture conditions are shown in Figure 13. Notably, plot *C* reveals a difference in the percentage of microglial cells exhibiting a hypertrophic morphology, with the coculture condition displaying a higher proportion of these cells across both groups. In contrast, the monoculture condition shows a consistently higher percentage of rodlike microglial cells under all three conditions compared to the cocultures (see plot *D* in Figure 13). These results further demonstrate that the presence of neurons significantly influences microglial morphology. This observation is supported by a visual comparison between confocal images of the monocultures (Figure A8, images *A*–*C*) and those of the cocultures (Figure 12, images *A*–*C*), where distinct morphological differences can be observed.

Additionally, the morphology results from a second coculture experiment using a different cell line (*CTRL1*) can be found in Figure A7 in the appendix. These results aligned well with those from the main experiment using cell line *WTSLi015-A*, further supporting the robustness of our cell model.

In summary, the morphology analysis demonstrates that culturing microglial cells in CSF influences their morphology. Specifically, microglia cultured in CSF exhibited more hypertrophic and ramified morphologies, suggesting that while they sense changes in their environment, these do not necessarily trigger a shift toward a highly phagocytic or amoeboid state. The results also highlight the significant impact of neurons on microglial morphology. Lastly, the results showed no morphological differences between the CTRL- and AD-group.

5.6 Comparative analysis

In this study, functional assays and qPCR were performed on monocultures of microglial cells, while the morphology analysis was conducted on cocultures consisting of cortical neurons and microglial cells. The results from the morphology analysis, particularly the comparison between monocultures and cocultures, showed that the presence of neurons clearly influences microglial morphology. This suggests that neurons likely impact other aspects of microglial behavior as well, such as viability, phagocytic activity, and gene expression. Consequently, it becomes challenging to directly compare the results from the functional assays and qPCR with those from the morphology analysis, as different culture systems were used.

However, one consistent observation across the phagocytosis assay, qPCR, and morphology analysis is that microglial cells are affected by being cultured in CSF compared to standard cell culture media. The phagocytosis assay demonstrated increased microglial phagocytic activity in the AD-group compared to the CTRL-group. Additionally, qPCR analysis revealed higher expression of the phagocytic gene *CD68* in microglia cultured in AD-CSF compared to those in CTRL-CSF. However, the morphology analysis did not show a great difference in the percentage of ameboid microglial cells in the AD-CSF compared to the CTRL-CSF.

The qPCR analysis revealed higher expression levels of the inflammatory genes *APOE* and *C1QA* in microglial cells cultured in AD-CSF compared to those cultured in CTRL-CSF. In the morphology analysis, a high proportion of hypertrophic microglial cells were observed in both CSF groups. Since the hypertrophic morphology is associated with microglial activation (see section 1.2.1), the findings from the qPCR and the morphology analysis suggest that the microglia become activated under these conditions. Additionally, the NULISA analysis showed a clear increase in *APOE* protein abundance in the AD-CSF compared to CTRL-CSF, further supporting the upregulation of the *APOE* gene in microglia cultured in AD-CSF.

In summary, these results indicate that microglial cells cultured in AD-CSF become more activated compared to CTRL-CSF. This activation is not reflected in the morphology analysis, where the highest proportion of microglial cells in both the AD- and CTRL-group displayed a ramified (homeostatic) morphology. However, both CSF-treated groups also showed a relatively high percentage of hypertrophic microglia (associated with activation), suggesting that the cells are indeed responding to stimuli in the CSF environment, however, they do not necessarily shift towards a phagocytic or amoeboid state.

5.7 Limitations

One limitation of this study is related to the preparation of the CSF-pools. Each pool consisted of only five individual patient samples, which may not fully represent the broader variability within the AD and control populations. Although the use of different pools across experiments provided a broader perspective on how varying CSF compositions affect microglial responses, it also introduces variability. This is because individual CSF samples can influence microglial cells differently. That can impact the results and be problematic when comparing the different experiments. Ideally, all CSF samples should have been pooled into one big pool, that then would have been used throughout the whole project. However, realistically, this is not possible, as new experiments are added along the way, increasing the demand of CSF that was not predictable at start of the project.

A second limitation relates to the control group. The CTRL-CSF samples were collected from elderly individuals, which could affect the outcome due to age-related changes in the composition of CSF. Aging can alter the levels of proteins, including Aβ and inflammatory markers, which could influence the comparison between AD-CSF and CTRL-CSF [53]. The CTRL-CSF could therefore contain higher levels of certain proteins, making the difference between AD-CSF and CTRL-CSF appear smaller. Additionally, CSF from younger individuals may have a different molecular composition, which could potentially reveal a clearer morphological difference between the AD and CTRL-group.

6 Future directions

Future experiments could investigate pHrodo-E.Coli uptake is more thoroughly conducted by conducting a CSF priming experiment. This would show whether the uptake patterns resemble those observed with pHrodo-Aβ, thereby providing further support for the hypothesis of competitive uptake. Additionally, examining the uptake of other disease-relevant substrates, such as tau tangles, could offer a more nuanced understanding of microglial phagocytic activity in the context of AD pathology. Furthermore, the cytotoxicity assay also needs to be repeated, as the initial results were inconclusive. A potential approach to improve this would be to perform a CSF priming experiment in which the CSF is removed and replaced with MiM prior to measuring LDH concentration. This would eliminate interference from LDH already present in the CSF, allowing for a more accurate assessment of cytotoxicity for the cell model.

In future research, it would be valuable to conduct similar morphological experiments at shorter exposure durations, such as 12 hours or less, as microglial activation might occur earlier than the 24-hour period used in this study. This could potentially reveal more distinct differences between the AD- and CTRL-CSF groups.

Another potential future approach would be to use CSF pools composed of a larger number of patient samples. This would help reduce the impact of individual variability, such as differences in overall health status, and thereby enhance the reliability of the results. However, such an expansion is currently constrained by the limited availability of patient-derived CSF. Furthermore, it would be interesting to do some live cell imaging to track microglial morphology transition over time in different conditions. That could capture more subtle states of activation. Additionally, one could combine the morphological analysis with single-cell RNA sequencing to link morphology to gene expression to give more information about microglial activation states.

7 Conclusions

The results from the cell viability assay, cytotoxicity assay, and Ki67 staining confirmed that the cell model was suitable for further experimentation, as CSF exposure had minimal effects on microglial proliferation and overall cell viability. The results from the NULISA experiment revealed differences in the relative abundance of the studied proteins between AD- and CTRL-CSF. However, noticeable variability was also observed between the individual pools within each group, which may have contributed to differences in experimental results as different CSF-pools may affect the microglial cells differently.

The qPCR results showed no significant differences between the CSF-groups, however, a trend toward higher gene expression in the AD-CSF group was observed for all the studied genes. This trend suggests that microglia exposed to AD-CSF may exist in a more activated state, even if the differences between CTRL-CSF and AD-CSF are relatively small. The phagocytosis assays provided further support for this interpretation. Microglial cells cultured in AD-CSF showed slightly increased uptake of pHrodo-Aβ for the CSF priming experiment. In contrast, the non-priming experiment for pHrodo-E.Coli indicates lower phagocytic activity in the AD-CSF compared to the other groups. These findings suggest that phagocytic activity may be modulated by the presence of competing substrates in the CSF, although further experiments, like CSF-priming with pHrodo-E.Coli, are needed to confirm this trend.

The morphology analysis showed significant differences between CSF- and CoM-treated groups but no clear differences between AD- and CTRL-CSF. Microglia cultured in CoM displayed a significantly higher percentage of amoeboid cells and fewer ramified cells, indicating a more activated, phagocytic state. This may be due to neuronal stress or damage in the CoM condition, which would trigger microglial activation. In contrast, neurons may thrive better in CSF, leading to a more homeostatic microglial phenotype. A comparison with monocultures supported the conclusion that the presence of neurons strongly influences microglial morphology.

In summary, the collective findings suggest that microglia exposed to AD-CSF exhibit signs of increased activation at the transcriptional and functional levels, although this is not strongly reflected in their morphology after 24 hours. Further experiments are required to improve the understanding of microglial morphology.

References

[1] Fangda Leng and Paul Edison. "Neuroinflammation and microglial activation in Alzheimer disease: where do we go from here?" In: *Nature Reviews Neurology* (). DOI: 10.1038/s41582-020-00435-y.

[2] Rosa C. Paolicelli et al. "Microglia states and nomenclature: A field at its crossroads". In: *Neuron* 110.21 (Nov. 2022), pp. 3458–3483. ISSN: 1097-4199. DOI: 10.1016/J.NEURON.2022.10.020.

[3] David M. Wilson et al. "Hallmarks of neurodegenerative diseases". In: *Cell* 186.4 (Feb. 2023), pp. 693–714. ISSN: 0092-8674. DOI: 10.1016/J.CELL.2022.12.032.

[4] Thomas C.T. Michaels et al. "Amyloid formation as a protein phase transition". In: *Nature Reviews Physics 2023 5:7* 5.7 (June 2023), pp. 379–397. ISSN: 2522-5820. DOI: 10.1038/s42254-023-00598-9. URL: https://www.nature.com/articles/s42254-023-00598-9.

[5] Jacob Aunstrup Larsen et al. "The mechanism of amyloid fibril growth from Φ-value analysis". In: *Nature Chemistry 2025 17:3* 17.3 (Jan. 2025), pp. 403–411. ISSN: 1755-4349. DOI: 10.1038/s41557-024-01712-9. URL: https://www.nature.com/articles/s41557-024-01712-9.

[6] Changlin Liu and Yong Zhang. "Nucleic acid-mediated protein aggregation and assembly". In: *Advances in Protein Chemistry and Structural Biology* 84 (2011), pp. 1–40. ISSN: 18761623. DOI: 10.1016/B978-0-12-386483-3.00005-7.

[7] National Institute of Health. *What Are the Signs of Alzheimer's Disease? — National Institute on Aging*. URL: https://www.nia.nih.gov/health/alzheimers-symptoms-and-diagnosis/what-are-signs-alzheimers-disease.

[8] Shanmugam Manoharan et al. "The Role of Reactive Oxygen Species in the Pathogenesis of Alzheimer's Disease, Parkinson's Disease, and Huntington's Disease: A Mini Review". In: *Oxidative Medicine and Cellular Longevity* 2016 (2016), p. 8590578. ISSN: 19420994. DOI: 10.1155/2016/8590578. URL: https://pmc.ncbi.nlm.nih.gov/articles/PMC5223034/.

[9] Fan Liu et al. "Effect of metal ions on Alzheimer's disease". In: *Brain and Behavior* 12.3 (Mar. 2022), e2527. ISSN: 21623279. DOI: 10.1002/BRB3.2527. URL: https://pmc.ncbi.nlm.nih.gov/articles/PMC8933773/.

[10] Lokesh A. Rukmangadachar and Pradeep C. Bollu. "Amyloid Beta Peptide". In: March (Aug. 2023), pp. 3–5. URL: https://www.ncbi.nlm.nih.gov/books/NBK459119/.

[11] Guo Fang Chen et al. "Amyloid beta: structure, biology and structure-based therapeutic development". In: *Acta Pharmacologica Sinica 2017 38:9* 38.9 (July 2017), pp. 1205–1235. ISSN: 1745-7254. DOI: 10.1038/aps.2017.28.

[12] Yoonsuk Cho et al. "Physiology and pharmacology of amyloid precursor protein". In: *Pharmacology & Therapeutics* 235 (July 2022), p. 108122. ISSN: 0163-7258. DOI: 10.1016/J.PHARMTHERA.2022.108122.

[13] Shorena Janelidze et al. "CSF Aβ42/Aβ40 and Aβ42/Aβ38 ratios: better diagnostic markers of Alzheimer disease". In: *Annals of Clinical and Translational Neurology* 3.3 (Mar. 2016), p. 154. ISSN: 23289503. DOI: 10.1002/ACN3.274. URL: https://pmc.ncbi.nlm.nih.gov/articles/PMC4774260/.

[14] Dongjoon Im and Tae Su Choi. "Distinctive contribution of two additional residues in protein aggregation of Aβ42 and Aβ40 isoforms". In: *BMB Reports* 57.6 (2024), p. 263. ISSN: 1976670X. DOI: 10.5483/BMBREP.2024-0044. URL: https://pmc.ncbi.nlm.nih.gov/articles/PMC11214890/.

[15] Amirreza Gholami. "Alzheimer's disease: The role of proteins in formation, mechanisms, and new therapeutic approaches". In: *Neuroscience Letters* 817 (Nov. 2023), p. 137532. ISSN: 0304-3940. DOI: 10.1016/J.NEULET.2023.137532.

[16] Constanze Depp et al. "Microglia transcriptional states and their functional significance: Context drives diversity". In: *Immunity* 58.5 (May 2025), pp. 1052–1067. ISSN: 1074-7613. DOI: 10.1016/J.IMMUNI.2025.04.009.

[17] Marco Colonna and Oleg Butovsky. "Microglia Function in the Central Nervous System During Health and Neurodegeneration". In: *Annual review of immunology* 35 (Apr. 2017), p. 441. ISSN: 15453278. DOI: 10.1146/ANNUREV-IMMUNOL-051116-052358.

[18] Shenrui Guo, Hui Wang, and Yafu Yin. "Microglia Polarization From M1 to M2 in Neurodegenerative Diseases". In: *Frontiers in Aging Neuroscience* 14 (Feb. 2022), p. 815347. ISSN: 16634365. DOI: 10.3389/FNAGI.2022.815347/FULL.

[19] Tabitha R.F. Green et al. "Reactive morphology of dividing microglia following kainic acid administration". In: *Frontiers in Neuroscience* 16 (Sept. 2022), p. 972138. ISSN: 1662453X. DOI: 10.3389/FNINS.2022.972138/FULL. URL: https://pmc.ncbi.nlm.nih.gov/articles/PMC9556904/.

[20] Pedro Réu et al. "The Lifespan and Turnover of Microglia in the Human Brain". In: *Cell Reports* 20.4 (July 2017), p. 779. ISSN: 22111247. DOI: 10.1016/J.CELREP.2017.07.004. URL: https://pmc.ncbi.nlm.nih.gov/articles/PMC5540680/.

[21] ALZFORUM. *TMEM119 — ALZFORUM*. URL: https://www.alzforum.org/alzantibodies/targets/tmem119.

[22] Samira Parhizkar and David M. Holtzman. "APOE mediated neuroinflammation and neurodegeneration in Alzheimer's disease". In: *Seminars in Immunology* 59 (Jan. 2022), p. 101594. ISSN: 1044-5323. DOI: 10.1016/J.SMIM.2022.101594.

[23] Wenjie Zhang, Yuan Chen, and Hui Pei. "C1q and central nervous system disorders". In: *Frontiers in Immunology* 14 (Mar. 2023), p. 1145649. ISSN: 16643224. DOI: 10.3389/FIMMU.2023.1145649/XML/NLM.

[24] Tabitha R F Green and Rachel K Rowe. "Quantifying microglial morphology: an insight into function". In: *Clinical and Experimental Immunology* 216 (2024), pp. 221–229. DOI: 10.1093/cei/uxae023.

[25] María Del Mar Fernández-Arjona et al. "Microglia Morphological Categorization in a Rat Model of Neuroinflammation by Hierarchical Cluster and Principal Components Analysis". In: (2017). DOI: 10.3389/fncel.2017.00235.

[26] Kenneth D. Harris and Gordon M.G. Shepherd. "The neocortical circuit: themes and variations". In: *Nature Neuroscience 2015 18:2* 18.2 (Jan. 2015), pp. 170–181. ISSN: 1546-1726. DOI: 10.1038/nn.3917.

[27] Byron K.Y. Bitanihirwe and Tsung Ung Wilson Woo. "Pyramidal neurons: physiology, pathophysiology, and postnatal development". In: *Factors Affecting Neurodevelopment: Genetics, Neurology, Behavior, and Diet* (Jan. 2021), pp. 433–445. DOI: 10.1016/B978-0-12-817986-4.00037-7.

[28] Jahangir Moini and Pirouz Piran. "Histophysiology". In: *Functional and Clinical Neuroanatomy* (2020), pp. 1–49. DOI: 10.1016/B978-0-12-817424-1.00001-X.

[29] Leian Chen et al. "The impact of Alzheimer's disease on cortical complexity and its underlying biological mechanisms". In: *Brain Research Bulletin* 225 (June 2025), p. 111320. ISSN: 0361-9230. DOI: 10.1016/J.BRAINRESBULL.2025.111320. URL: https://www.sciencedirect.com/science/article/pii/S0361923025001327.

[30] Jefferson W. Kinney et al. "Inflammation as a central mechanism in Alzheimer's disease". In: *Alzheimer's and Dementia: Translational Research and Clinical Interventions* 4 (Jan. 2018), pp. 575–590. ISSN: 23528737. DOI: 10.1016/J.TRCI.2018.06.014.

[31] Trevor Huff et al. "Neuroanatomy, Cerebrospinal Fluid". In: *StatPearls* (Aug. 2023). URL: https://www.ncbi.nlm.nih.gov/books/NBK470578/.

[32] Gemma Salvadó et al. "Disease staging of Alzheimer's disease using a CSF-based biomarker model". In: *Nature Aging 2024 4:5* 4.5 (Mar. 2024), pp. 694–708. ISSN: 2662-8465. DOI: 10.1038/s43587-024-00599-y. URL: https://www.nature.com/articles/s43587-024-00599-y.

[33] National Institute of Aging. *How Is Alzheimer's Disease Diagnosed? — National Institute on Aging*. URL: https://www.nia.nih.gov/health/alzheimers-symptoms-and-diagnosis/how-alzheimers-disease-diagnosed.

[34] Linda Karlsson et al. "Cerebrospinal fluid reference proteins increase accuracy and interpretability of biomarkers for brain diseases". In: *Nature Communications 2024 15:1* 15.1 (May 2024), pp. 1–15. ISSN: 2041-1723. DOI: 10.1038/s41467-024-47971-5. URL: https://www.nature.com/articles/s41467-024-47971-5.

[35] Yichen Shi, Peter Kirwan, and Frederick J. Livesey. "Directed differentiation of human pluripotent stem cells to cerebral cortex neurons and neural networks". In: *Nature Protocols 2012 7:10* 7.10 (Sept. 2012), pp. 1836–1846. ISSN: 1750-2799. DOI: 10.1038/nprot.2012.116.

[36] Wei Feng et al. "NULISA: a proteomic liquid biopsy platform with attomolar sensitivity and high multiplexing". In: *Nature Communications 2023 14:1* 14.1 (Nov. 2023), pp. 1–14. ISSN: 2041-1723. DOI: 10.1038/s41467-023-42834-x. URL: https://www.nature.com/articles/s41467-023-42834-x.

[37] *kajsahal/Masterthesis at Morphology*. URL: https://github.com/kajsahal/Masterthesis/tree/Morphology.

[38] Thermo Fisher Scientific. *CyQUANT ™ XTT Cell Viability Assay — 2*. Tech. rep. URL: www.thermofisher.com/us/en/home/global/terms-and-conditions.html..

[39] Thermo Fisher Scientific. *CyQUANT LDH Cytotoxicity Assay Kit Product Information Sheet (Pub.No. MAN0018500 B.0)*. Tech. rep. URL: www.thermofisher.com/us/en/home/global/terms-and-conditions.html..

[40] National Library of Medicine. *ACTB actin beta [Homo sapiens (human)] - Gene - NCBI*. URL: https://www.ncbi.nlm.nih.gov/gene/60.

[41] FUJIFILM Cellular Dynamics. *iCell ® Microglia Application Protocol Labeling Amyloid Beta with pHrodo Red*. Tech. rep. URL: https://fujifilmcdi.com/assets/CDI_iCellMGL_Incucyte_AP.pdf.

[42] Amicia D. Elliott. "Confocal Microscopy: Principles and Modern Practices". In: *Current protocols in cytometry* 92.1 (Mar. 2020), e68. ISSN: 19349300. DOI: 10.1002/CPCY.68.

[43] Jennifer Kim, Paul Pavlidis, and Annie Vogel Ciernia. "Development of a High-Throughput Pipeline to Characterize Microglia Morphological States at a Single-Cell Resolution". In: *eNeuro* 11.7 (July 2024). ISSN: 2373-2822. DOI: 10.1523/ENEURO.0014-24.2024.

[44] *DHARMa: residual diagnostics for hierarchical (multi-level/mixed) regression models*. URL: https://cran.r-project.org/web/packages/DHARMa/vignettes/DHARMa.html.

[45] Jung Soo Park et al. "Cerebrospinal fluid lactate dehydrogenase as a potential predictor of neurologic outcomes in cardiac arrest survivors who underwent target temperature management". In: *Journal of Critical Care* 57 (June 2020), pp. 49–54. ISSN: 0883-9441. DOI: 10.1016/J.JCRC.2020.02.001.

[46] Andrea Sturchio et al. "High cerebrospinal amyloid-β 42 is associated with normal cognition in individuals with brain amyloidosis". In: (2021). DOI: 10.1016/j.eclinm.2021.100988. URL: https://doi.org/10.1016/j.eclinm.2021.100988.

[47] Vincent Bouteloup et al. "Explaining the Variability of Alzheimer Disease Fluid Biomarker Concentrations in Memory Clinic Patients Without Dementia". In: *Neurology* 102.8 (Mar. 2024), e209219. ISSN: 1526632X. DOI: 10.1212/WNL.0000000000209219/SUPPL{_}FILE/SUPPLEMENTARY{_}TABLE2.PDF.

[48] Michael John Dolan et al. "Exposure of iPSC-derived human microglia to brain substrates enables the generation and manipulation of diverse transcriptional states in vitro". In: *Nature Immunology 2023 24:8* 24.8 (July 2023), pp. 1382–1390. ISSN: 1529-2916. DOI: 10.1038/s41590-023-01558-2.

[49] Francesca Fagiani et al. "A glia-enriched stem cell 3D model of the human brain mimics the glial-immune neurodegenerative phenotypes of multiple sclerosis". In: *Cell Reports Medicine* 5.8 (Aug. 2024), p. 101680. ISSN: 2666-3791. DOI: 10.1016/J.XCRM.2024.101680.

[50] Julia Izsak et al. "Human Cerebrospinal Fluid Promotes Neuronal Circuit Maturation of Human Induced Pluripotent Stem Cell-Derived 3D Neural Aggregates". In: *Stem Cell Reports* 14.6 (June 2020), p. 1044. ISSN: 22136711. DOI: 10.1016/J.STEMCR.2020.05.006. URL: https://pmc.ncbi.nlm.nih.gov/articles/PMC7355159/.

[51] Christopher N. Parkhurst and Wen Biao Gan. "Microglia dynamics and function in the CNS". In: *Current opinion in neurobiology* 20.5 (Oct. 2010), p. 595. ISSN: 09594388. DOI: 10.1016/J.CONB.2010.07.002. URL: https://pmc.ncbi.nlm.nih.gov/articles/PMC3708473/.

[52] Tabitha R.F. Green and Rachel K. Rowe. "Quantifying microglial morphology: an insight into function". In: *Clinical and Experimental Immunology* 216.3 (May 2024), pp. 221–229. ISSN: 13652249. DOI: 10.1093/CEI/UXAE023. URL: https://dx.doi.org/10.1093/cei/uxae023.

[53] Carl P.C. Chen, Ruo Li Chen, and Jane E. Preston. "The influence of ageing in the cerebrospinal fluid concentrations of proteins that are derived from the choroid plexus, brain, and plasma". In: *Experimental Gerontology* 47.4 (Apr. 2012), pp. 323–328. ISSN: 0531-5565. DOI: 10.1016/J.EXGER.2012.01.008.

A1 Methods

Cell media

Table A1 presents the content of the cell media used in the study.

Table A1: Content of the cell media used in the study.

mTESR+	Advanced DMEM/F12 supplemented with 10μ/mL GlutaMAX, 10μ/mL PEST, and 1.5μ/mLβ-mercaploethanol
EBM	mTeSR1 media supplemented with 10 μM ROCK inhibitor, 50 ng/mL BMP-4, 20 ng/mL, SCF and 50 ng/mL VEGF-121
HM	mTeSR1 media supplemented with 100 ng/mL M-CSF and 25 ng/mL IL-3
MiM	mTeSR1 media supplemented with 100 ng/mL IL-34 and 10 ng/mL GM-CSF
NMM	DMEM, N2 (1:100), Insulin (5μg/mL), Glutamax (1:100), NEAA (100 μM), 2-mercaptoethanol (100 μM), pencillin (50 U/mL), streptomycin (50 mg/mL), B72 (with vitamin A)(1:50) and neurobasal media WO phenol red
CoM	NMM supplemented with 1μL IL34/ml NMM and 1μL GM-CSF/ml NMM

Validation of cell model

Figure A1 shows the plate layout of one of the cell viability assays conducted.

	1	2	3	4	5	6	7	8	9	10	11	12
A												
B			MiM	CTRL	AD							
C			MiM	CTRL	AD							
D												
E												
F												
G												
H												

Figure A1: Plate layout for the first microglial cell viability assay with duplicates of each group.

Figure A2 shows the plate layout of the cytotoxicity assays conducted.

	1	2	3	4	5	6	7	8	9	10	11	12
A												
B			MiM	CTRL	AD	Spontaneous LDH activity	Max LDH activity	Positive control				
C			MiM	CTRL	AD	Spontaneous LDH activity	Max LDH activity	Positive control				
D			MiM	CTRL	AD	Spontaneous LDH activity	Max LDH activity	Positive control				
E												
F												
G												
H												

Figure A2: Plate layout for the first microglial cytotoxicity assay with a triplicate of each group.

Phagocytosis assay

Figure A3 shows the plate layout of the concentration optimization experiment conducted for the phagocytosis assays.

	1	2	3	4	5	6	7	8	9	10	11	12
A												
B		Blank	1	2.5	5							
C		Blank	1	2.5	5							
D												
E												
F												
G												
H												

	1	2	3	4	5	6	7	8	9	10	11	12
A												
B		Blank	0.5	1	2	5	0.25					
C		Blank	0.5	1	2	5	0.25					
D												
E												
F												
G												
H												

Figure A3: Plate layout for concentration optimization for pHrodo-E.Coli (left) and pHrodo-$A\beta$ (right)

Figure A4 shows the plate layout of the time optimization experiment conducted for the phagocytosis assays.

	1	2	3	4	5	6	7	8	9	10	11	12
A												
B		AD (48h)	AD (48h)	AD (48h)	AD (48h)	AD (24h)	AD (24h)	AD (24h)	AD (24h)	BLANK		
C		CTRL (48h)	CTRL (48h)	CTRL (48h)	CTRL (48h)	CTRL (24h)	CTRL (24h)	CTRL (24h)	CTRL (24h)	BLANK		
D		MiM (48h)	MiM (48h)	MiM (48h)	MiM (48h)	MiM (24h)	MiM (24h)	MiM (24h)	MiM (24h)	BLANK		
E												
F												
G												
H												

Figure A4: Plate layout of time optimization phagocytosis assay using pHrodo-E.Coli

Figure A5 shows the plate layout of the phagocytosis assays conducted using pHrodo-E.Coli and pHrodo-$A\beta$.

	1	2	3	4	5	6	7	8	9	10	11	12
A												
B				Blank	MiM	CTRL	AD					
C				Blank	MiM	CTRL	AD					
D				Blank	MiM	CTRL	AD					
E												
F												
G												
H												

Figure A5: Plate layout of the microglial phagocytosis assay using pHrodo-E.Coli and pHrodo-$A\beta$

Figure A6 shows the plate layout of the CSF priming phagocytosis assay conducted using pHrodo-E.Coli and pHrodo-$A\beta$.

	1	2	3	4	5	6	7	8	9	10	11	12
A												
B			MiM	CTRL	AD							
C			MiM	CTRL	AD							
D												
E												
F												
G												
H												

Figure A6: Plate layout of the microglial phagocytosis assay using pHrodo-$A\beta$ with CSF priming

Morphology analysis

For the confocal microscope, the following settings were used to capture the three-channel images (see Table A2). In addition, the pinhole was set to 1.0 and the averaging (AV) to 1.2. For the z-stack images, five steps were acquired with 0.875 μm spacing between each step, covering a total range of 3.5 μm.

Table A2: Settings for the three channels used during image acquisition with the confocal microscope.

	HV	**Offset**	**Wavelength**
DAPI	60	0	1.54
Alexa 488	20	0	1.08
Alexa 568	40	0	1.54

A2 Results

Below are some additional results from the morphology analysis.

Morphology analysis

Figure A7 shows the results from the morphology analysis conducted on the second coculture using the *CTRL1* cell line.

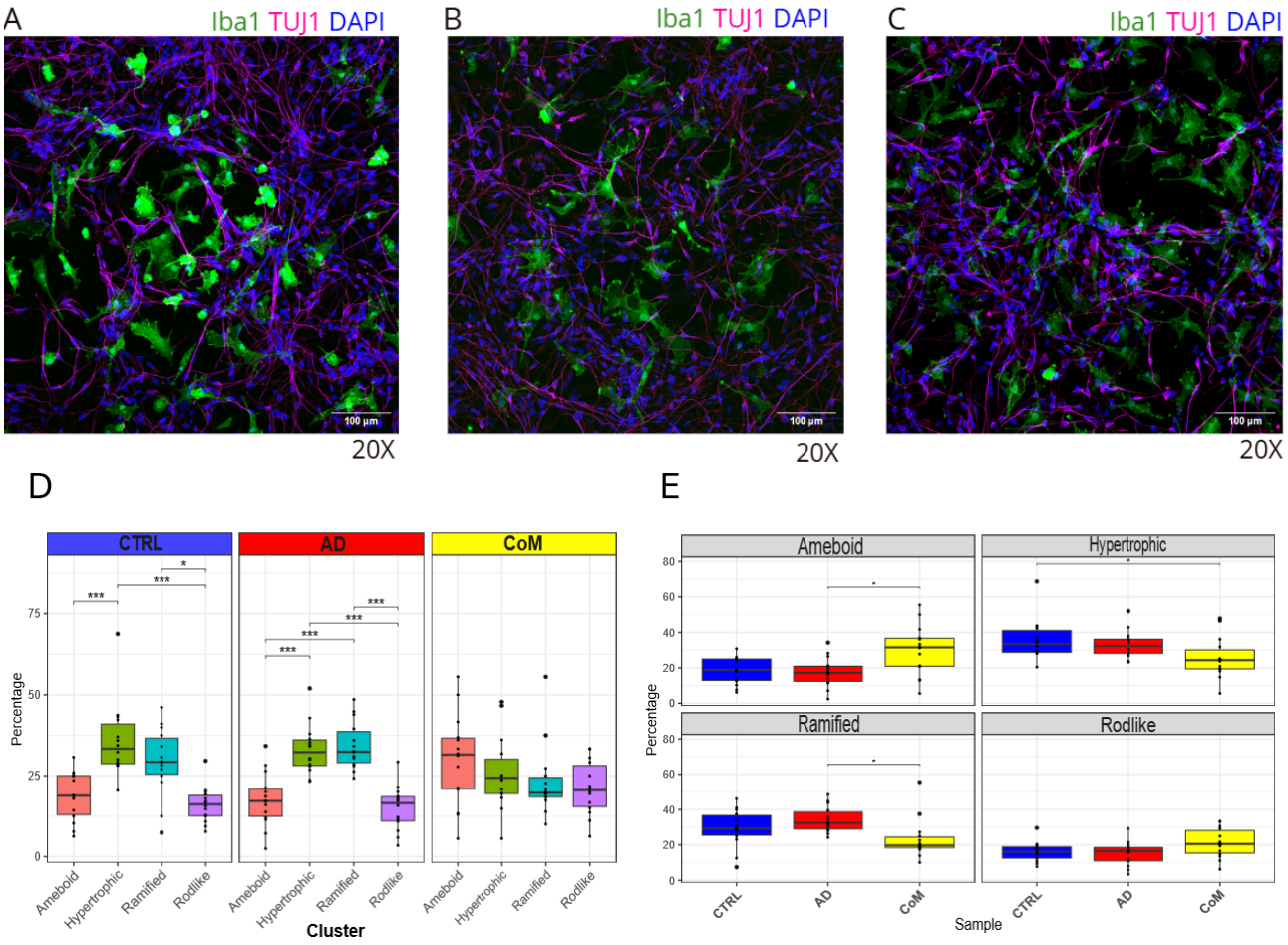

Figure A7: ***A)*** Image of a coculture (*CTRL1*) cultured in CoM for 24 hours, taken in a confocal microscope. ***B)*** Image of a coculture (*CTRL1*) cultured in CTRL-CSF for 24 hours, taken in a confocal microscope. ***C)*** Image of a coculture (*CTRL1*) cultured in AD-CSF for 24 hours, taken in a confocal microscope. ***D)*** A boxplot over each group's percentages of microglia cells with amoeboid, hypertrophic, ramified, and rodlike morphology. Asterisks indicate statistically significant differences between groups (p ¡ 0.05 = *, p ¡ 0.01 = **, p ¡ 0.001 = ***). ***E)*** A boxplot over each group's percentages of microglia cells with amoeboid, hypertrophic, ramified, and rodlike morphology. Asterisks indicate statistically significant differences between groups (p ¡ 0.05 = *, p ¡ 0.01 = **, p ¡ 0.001 = ***).

Images *A*, *B*, and *C* in Figure A7 show representative images of the cocultures taken with the confocal microscope. Plots *D* and *E* show a higher percentage of ramified and hypertrophic microglia in the CSF-groups compared to the CoM-group. The percentage of ameboid microglia is significantly higher in the CoM-group than in the AD-group. Additionally, there is a significant increase in hypertrophic microglia in the CTRL-group compared to CoM, as well as a significant increase in ramified microglia in the AD-group compared to CoM.

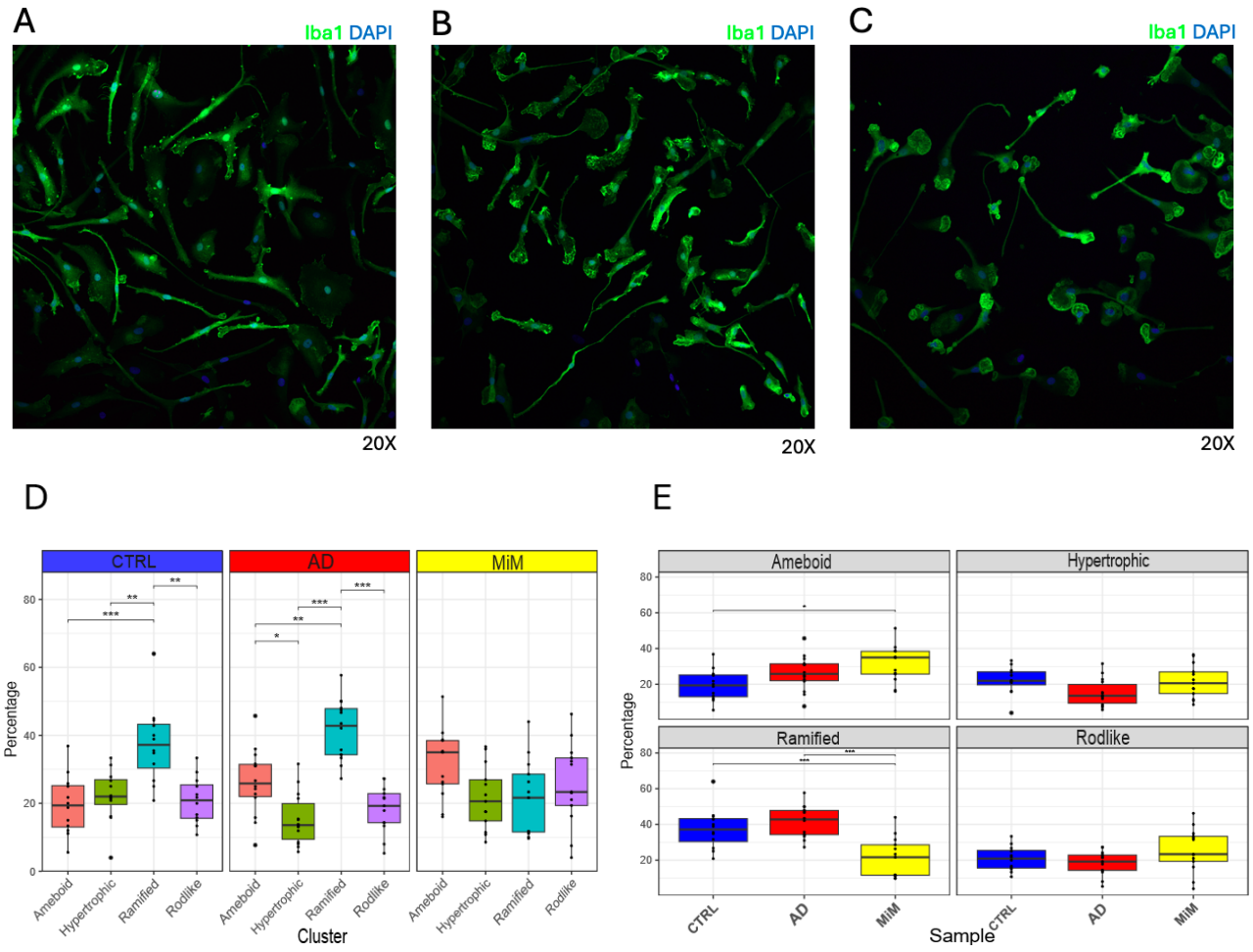

Figure A8: ***A)*** Image of a monoculture (*WTSLi015-A*) cultured in CoM for 24 hours, taken in a confocal microscope. ***B)*** Image of a monoculture (*WTSLi015-A*) cultured in CTRL-CSF for 24 hours, taken in a confocal microscope. ***C)*** Image of a monoculture (*WTSLi015-A*) cultured in AD-CSF for 24 hours, taken in a confocal microscope. ***D)*** A boxplot over each group's percentages of microglia cells with amoeboid, hypertrophic, ramified, and rodlike morphology. Asterisks indicate statistically significant differences between groups (p ¡ 0.05 = *, p ¡ 0.01 = **, p ¡ 0.001 = ***). ***E)*** A boxplot over each group's percentages of microglia cells with amoeboid, hypertrophic, ramified, and rodlike morphology. Asterisks indicate statistically significant differences between groups (p ¡ 0.05 = *, p ¡ 0.01 = **, p ¡ 0.001 = ***).

Figure A8 presents the results of the morphology analysis conducted on the monoculture using the *WTSLi015-A* cell line. The MiM-group exhibits a higher percentage of ameboid microglia compared to both the AD- and CTRL-groups, with a significant increase observed between the MiM- and CTRL-groups. Both the AD- and CTRL-groups display a higher percentage of ramified microglia, with the AD-group showing the highest proportion. The percentage of hypertrophic microglia is greater in the CTRL-group compared to the AD-group.

DEPARTMENT OF SOME SUBJECT OR TECHNOLOGY
CHALMERS UNIVERSITY OF TECHNOLOGY
Gothenburg, Sweden
www.chalmers.se

CHALMERS
UNIVERSITY OF TECHNOLOGY